CHAPTER VI

Reduced graphene oxide (rGO)/PEDOT:PSS/Nickel Manganite (NiMn$_2$O$_4$) ternary nanocomposite as anode catalyst for methanol oxidation

6.1 Introduction

Intense research efforts are going worldwide on transition metal oxide based electrocatalysts for their applications in direct methanol fuel cell [1]. Recently, mixed transition metal oxides are gaining much attention of the researchers, which can be synthesized by combining two versatile transition metal oxides. These single-phase mixed transition metal oxides are a new class of electroactive material, and are extensively used in energy related systems [2-6]. The mixed transition metal oxides are of AB$_2$O$_4$ spinel structure, where, cubic close packed O^{2-} and A^{2+} occupy 1/8th of the tetrahedral voids and B^{3+} occupies 1/2 of the octahedral voids [7]. Mixed transition metal oxides-based nanocomposites exhibit much enhanced electrocatalytic performance such as chemical reactivity, anti-poisoning activity and stability than that of individual components [1]. Among all the mixed transition metal oxides, NiMn$_2$O$_4$ is having for its rich redox active sites, high conductivity, low-cost, easy preparation, structural stability and environmentally benign [2, 8]. Various factors including morphology, structure of the crystal, surface area, rate of ion transport and valence states of redox active ions of the electrocatalyst determine electroactivity of the catalyst [7]. Porous structure of electrode material helps in enhancement of ion transport process by generating many electroactive sites within the electrocatalyst material. Therefore, proper design and nanostructuring of electrode material is very necessary to exploit all the properties of the material. However, the applications of NiMn$_2$O$_4$ are limited by low surface area, poor conductivity and low dispersity [2]. Therefore, carbon materials are incorporated with NiMn$_2$O$_4$ in order to overcome these drawbacks.

Low redox potential (-0.6 eV), high electrical conductivity (300 S cm^{-1}) and wide potential window (1.2-1.5 V) of PEDOT enhance the electrochemical kinetics of

methanol oxidation. In spite of having these enormous features, the poor solubility of PEDOT is a serious issue for its practical application in devices. Therefore, a polyelectrolyte, poly(styrene sulfonic acid) (PSS) is added to PEDOT to overcome the solubility problem and forming PEDOT:PSS [9]. However, the presence of PSS decreases electrical conductivity of the polymer PEDOT, which affects its applicability as an electrocatalyst in DMFC. Therefore, carbon allotropes, metal nanoparticles, metal oxides are incorporated to enhance conductivity of the system. A high electrocatalytic activity is observed for methanol oxidation at reduced graphene oxide supported (CoFeNi)$_9$S$_8$ nanoparticles (CFNS/rGO) modified glassy carbon electrode in alkaline media [10]. The considerable amount of electrocatalytic activity of CFNS/rGO nanocomposite is attributed to the synergic effects of Co, Fe, and Ni, large surface area and porosity of rGO and good dispersion of CFNS nanoparticles over rGO nanosheet.

Carbon nanomaterials hybridized with transition metal oxides exhibit improved electrochemical performance due to presence of redox states, facilitating fast charge transfer at the electrode-electrolyte interface. In another work, NiCo$_2$O$_4$ nanorods loaded rGO (NiCo$_2$O$_4$/rGO) catalyst shows excellent electrocatalytic performance with the peak current densities of 9.6 mA cm^{-2} at 290 K and 16.2 mA cm^{-2} at 310 K in alkaline solution due to the synergetic effect of Ni^{2+} and Co^{3+} ions and high electrical conductivity of rGO [11]. Synergetic effects of rGO nanosheets and transition metal oxides in the nanocomposites can be explained as follows [12]: (i) rGO provides 2D support for dispersing metal oxides and maintains the size and shape of the metal oxides; (ii) metal oxides behave as nanospacer between rGO layers that prevents re-stacking among the layers; (iii) conductive porous network of rGO sheets enhances the charge transfer process in metal oxides; (iv) rGO nanosheets prevent the change in volume and agglomeration of metal oxides; (v) the remaining functional units including hydroxyl, carboxyl, carbonyl at the edges and basal planes of rGO layers as a result of chemical reduction ensure strong interfacial interactions and electrical contacts between rGO and metal oxides.

This chapter reports the development of ternary nanocomposite of a mixed transition metal oxide NiMn$_2$O$_4$ having two redox centres with PEDOT:PSS and rGO. The presence of two redox centres in NiMn$_2$O$_4$ is likely to significantly improve the electrocatalytic activity as compared to that of single transition metal oxide. rGO/PEDOT:PSS/NiMn$_2$O$_4$/ITO electrode exhibits enhanced anodic peak current density of 70.4 mA cm^{-2} while lower onset voltage of 0.21 V in presence of 0.5 M methanol

containing in 0.5 M NaOH electrolyte than that of PEDOT:PSS/NiMn$_2$O$_4$/ITO and NiMn$_2$O$_4$/ITO electrodes. Moreover, rGO/PEDOT:PSS/NiMn$_2$O$_4$/ITO electrode shows higher cyclic stability with a current retention of 77.4% in 0.5 M methanol solution after 1000 CV cycles. The presence of rGO nanosheets increases the electrical conductivity and offers large surface area for methanol oxidation and the presence of PEDOT:PSS prevents aggregation of NiMn$_2$O$_4$ nanoparticles.

6.2 Morphological characterizations

6.2.1 Scanning electron microscopy

Morphological investigations of NiMn$_2$O$_4$, PEDOT:PSS/NiMn$_2$O$_4$ and rGO/PEDOT:PSS/NiMn$_2$O$_4$ nanocomposites have been done by SEM as shown in Figure 6.1. The SEM image of NiMn$_2$O$_4$ (Figure 6.1 (i)) reveals granular porous structure with large number of mesopores, which arise due to the growth of fine NiMn$_2$O$_4$ nanoparticles. Moreover, the gases released during calcinations of nickel-manganese hydroxide nanoparticles lead to the agglomeration of material and thus formation of secondary porous material [1]. Figure 6.1 (ii) displays porous network of polymer coated NiMn$_2$O$_4$ with larger surface area, while in Figure 6.1 (iii), wrinkle like appearance is observed upon incorporation of rGO in the ternary nanocomposite. Moreover, the polymer coated NiMn$_2$O$_4$ nanostructures are enclosed within rGO nanosheets; therefore these nanostructures are no longer visible in rGO/PEDOT:PSS/NiMn$_2$O$_4$ nanocomposite. Composition of rGO/PEDOT:PSS/NiMn$_2$O$_4$ nanocomposite has been investigated by EDX analysis. In Figure 6.1 (iv), the appearance of C, O, S, Mn and Ni peaks confirms successful synthesis of rGO/PEDOT:PSS/NiMn$_2$O$_4$ nanocomposite. Quantitative analysis from EDX displays that the nanocomposite contains 53.19 wt.% of C, 32.07 wt.% of O, 6.49 wt.% of S, 0.87 wt.% of Mn, and 7.38 wt.% of Ni. The elemental mapping has been carried out to observe the distribution of C, O, S, Mn and Ni in the ternary nanocomposite. Figures 6.1 (v) to (ix) represent elemental mapping of C, O, S, Mn and Ni in rGO/PEDOT:PSS/NiMn$_2$O$_4$ nanocomposite, respectively. Higher percentage of carbon is due to the presence of both polymer PEDOT:PSS and rGO nanosheets. The uniform distribution of Ni and Mn over rGO nanosheet and PEDOT:PSS matrix enhances electrocatalytic activity of the nanocomposite.
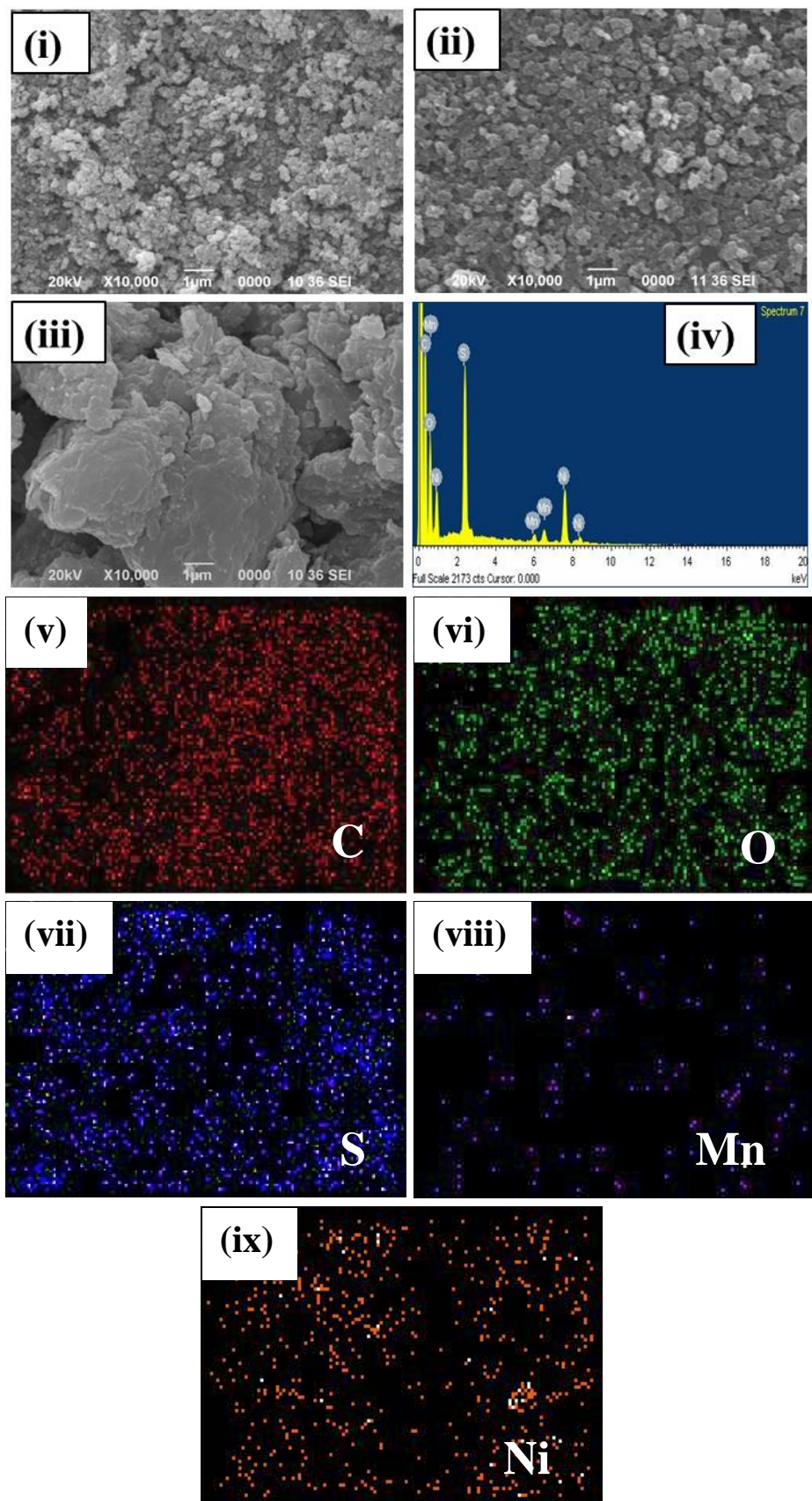
Figure 6.1: *SEM micrographs of (i) NiMn$_2$O$_4$, (ii) PEDOT:PSS/NiMn$_2$O$_4$ and (iii) rGO/PEDOT:PSS/NiMn$_2$O$_4$ nanocomposites. (iv) EDX spectrum of*

rGO/PEDOT:PSS/NiMn$_2$O$_4$ nanocomposite. EDX mapping of rGO/PEDOT:PSS/NiMn$_2$O$_4$ nanocomposite showing the distribution of elements (v) C, (vi) O, (vii) S, (viii) Mn and (ix) Ni.
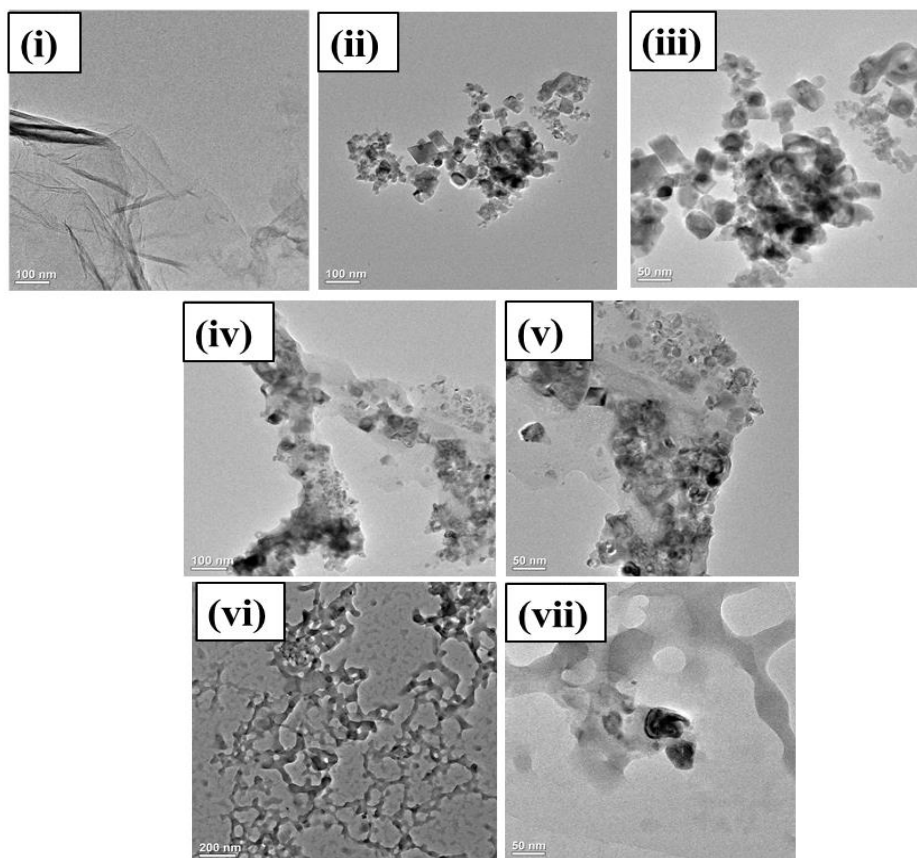
6.2.2 Transmission electron microscopy

Figure 6.2: TEM micrographs of (i) rGO nanosheet, (ii) and (iii) NiMn$_2$O$_4$ nanoparticles, (iv) and (v) PEDOT:PSS/NiMn$_2$O$_4$ nanocomposite, (vi) and (vii) rGO/PEDOT:PSS/NiMn$_2$O$_4$ nanocomposite.

TEM has been performed for in depth morphological analysis of all the synthesized samples as displayed in Figure 6.2. Figure 6.2 (i) shows wrinkled sheet like structures of rGO nanosheets. The TEM images (Figures 6.2 (ii) and (iii)) of NiMn$_2$O$_4$ reveal the formation of spherical nanoparticles. NiMn$_2$O$_4$ nanoparticles have been synthesized in precisely optimized reaction conditions to control size of the particles, however diameter of all the synthesized particles are not identical and lies within the range from 35 to 40 nm. In case of PEDOT:PSS/NiMn$_2$O$_4$ nanocomposite, the homogenous dispersion of NiMn$_2$O$_4$ particles within the polymer matrices has been observed as shown in Figures

6.2 (iv) and (v). The TEM micrographs (Figures 6.2 (vi) and (vii)) of rGO/PEDOT:PSS/NiMn$_2$O$_4$ nanocomposite display a porous structure, where PEDOT:PSS coated NiMn$_2$O$_4$ particles are embedded within interconnected network of rGO sheets.

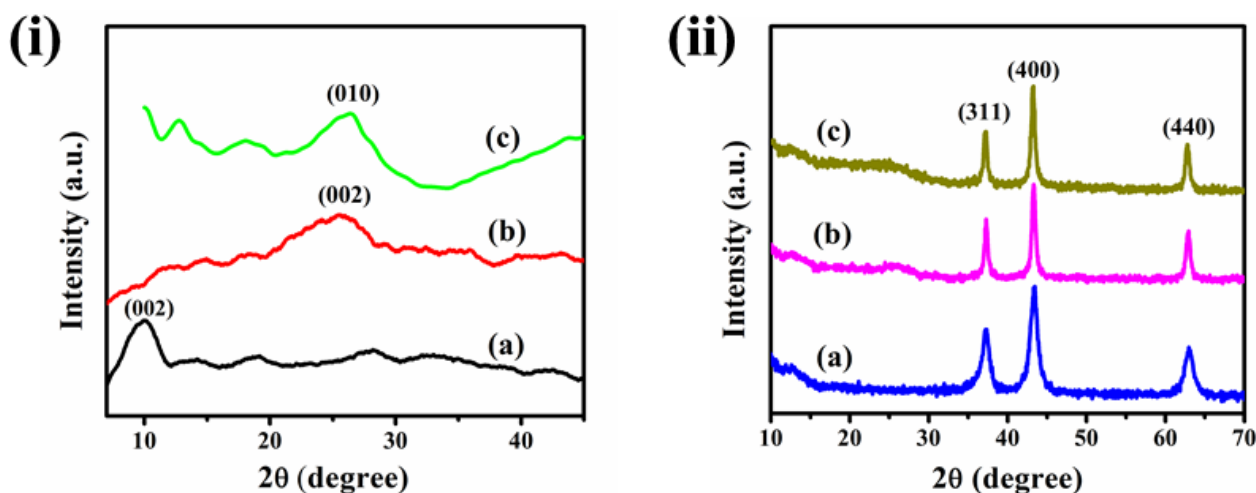## 6.3 Physical Characterizations

6.3.1 X-ray diffraction

Figure 6.3: *(i) XRD patterns of (a) GO, (b) rGO and (c) PEDOT:PSS, (ii) XRD patterns of (a) NiMn$_2$O$_4$, (b) PEDOT:PSS/NiMn$_2$O$_4$ nanocomposite and (c) rGO/PEDOT:PSS/NiMn$_2$O$_4$ nanocomposite.*

The XRD patterns of GO, rGO, PEDOT:PSS, NiMn$_2$O$_4$, PEDOT:PSS/NiMn$_2$O$_4$ and rGO/PEDOT:PSS/NiMn$_2$O$_4$ nanocomposites are displayed in Figure 6.3. An intense diffraction peak of GO appears at 10° assigned to (002) plane with large inter-planar spacing (d) of 0.87 nm due to incorporation of oxygen functional units between the graphite layers [13]. The XRD peak of GO related to (002) plane shifts to 25.5^o in case of rGO. The shift in XRD peak with decrease in d value of 0.34 nm owing to deformation of long range order of rGO planes during exfoliation of GO. The decrease in d value in rGO compared to GO indicates the presence of π-π interaction among the nanosheets and partial elimination of oxygen containing groups [13]. The diffraction peaks in PEDOT:PSS are observed at 2θ positions of 12.8^o, 18° and 26.2^o corresponding to the d-spacings of 6.9, 4.9 and 3.3 Å, respectively. The low intensity peaks of PEDOT:PSS around 12.8^o and 18° arise due to reflection from second order lattice plane (200) and

amorphous PSS chain structure, respectively [14]. Moreover, one broad peak at 26.2^{o} appears due to interchain π-π stacking distance between (010) planes [14]. The characteristic peaks of $NiMn_2O_4$ appear at 37.1^{o}, 43.2^{o} and 62.6^{o}, which can be attributed to (311), (400) and (440) planes of $NiMn_2O_4$, respectively [8]. The XRD pattern of PEDOT:PSS/$NiMn_2O_4$ nanocomposite exhibits all the characteristic peaks of $NiMn_2O_4$ along with a small intense peak around 26° indicating incorporation of the polymer PEDOT:PSS. In curve c of Figure 6.3 (ii), a broad XRD peak is observed around 25.3^{o} demonstrating the addition of rGO in rGO/PEDOT:PSS/$NiMn_2O_4$ nanocomposite. However, diffraction peaks of disordered rGO and amorphous PEDOT:PSS are much weaker in comparison to that of crystalline $NiMn_2O_4$. The XRD pattern of ternary nanocomposite ensures the presence of all the three materials i.e. rGO, PEDOT:PSS and $NiMn_2O_4$.
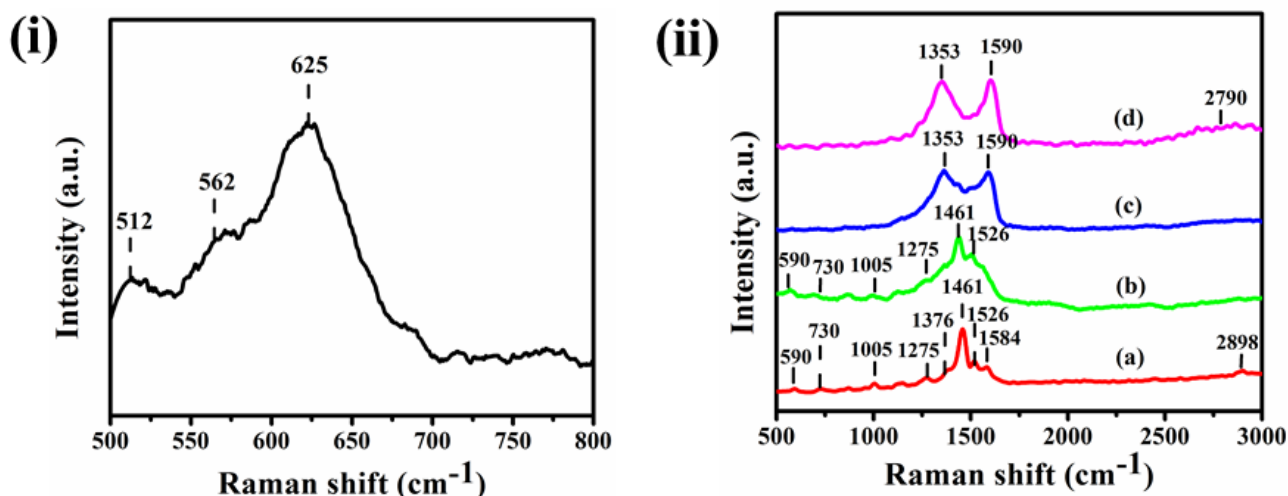
6.3.2 Raman spectroscopy

Figure 6.4: (i) Raman spectrum of NiMn₂O₄, (ii) Raman spectra of (a) PEDOT:PSS, (b) PEDOT:PSS/NiMn₂O₄ nanocomposite, (c) rGO/PEDOT:PSS/NiMn₂O₄ nanocomposite and (d) rGO.

Raman spectroscopy is a widely used tool to analyse the structural properties such as defects and disorders present in materials. Figures 6.4 (i) and (ii) display Raman spectra of as synthesized $NiMn_2O_4$, PEDOT:PSS, PEDOT:PSS/$NiMn_2O_4$, rGO/PEDOT:PSS/$NiMn_2O_4$ nanocomposites and rGO. The Raman spectra of $NiMn_2O_4$ in Figure 6.4 (i) displays three bands: first band at 625 cm^{-1} is attributed to A_{1g} active

mode related to asymmetric Mn-O stretching vibration mode of MnO$_6$ unit, the second band at 562 cm^{-1} is assigned to F$_{2g}$ mode and the third peak at 512 cm^{-1} is ascribed to Ni-O stretching vibration mode in NiMn$_2$O$_4$ [15, 16]. The characteristic Raman signature peaks for PEDOT:PSS can be explained as: The C-S aliphatic stretching vibration modes of PSS are centered at 590, 730 and 1005 cm^{-1} [17]. One intense peak centred about 1461 cm^{-1} corresponds to C$_\alpha$=C$_\beta$ symmetrical stretching vibration [18]. The other two Raman bands centred at 1526 cm^{-1} and 1584 cm^{-1} are attributed to the C$_\alpha$= C$_\beta$ asymmetrical stretching vibration and associated with thiophene rings in the middle and at the end of PEDOT chains, respectively [18]. Other significant peaks of PEDOT:PSS centred at 1376 and 1275 cm^{-1} appear due to C$_\beta$-C$_\beta$ stretching deformations and C$_\alpha$-C$_\alpha$ inter ring stretching vibrations, respectively [19]. Moreover, one small band is observed at 2898 cm^{-1} because of the presence of C-H bond stretching vibration [20]. Both rGO nanosheet and rGO/PEDOT:PSS/NiMn$_2$O$_4$ nanocomposite show significant D and G bands at 1353 and 1590 cm^{-1}, respectively. The D-band, attributed to breathing modes of six atom carbon rings with A$_{1g}$ symmetry is Raman active only in presence of defects and disorder in carbon materials [21]. The G-band appears due to first order scattering from high frequency E$_{2g}$ phonon modes of sp^2 hybridized C atoms in rGO sheets [22]. In case of rGO nanosheets, characteristic 2D band is observed around 2790 cm^{-1} attributing to the double resonance transitions [23]. The higher Raman intensity of G band than that of 2D band indicates the presence of multilayered rGO nanosheets.

6.3.3 X-ray photoelectron spectroscopy

XPS has been carried out to investigate the surface composition, chemical oxidation and electronic states of rGO/PEDOT:PSS/NiMn$_2$O$_4$ nanocomposite. The XPS spectra of ternary nanocomposite have been displayed in Figure 6.5. The clearly visible peaks in the survey spectrum (Figure 6.5(i)) of rGO/PEDOT:PSS/NiMn$_2$O$_4$ nanocomposite within the range from 0 to 1350 eV indicate that the nanocomposite contains C, O, S, Ni and Mn elements. Moreover, significant peaks of C, O, Mn and Ni are observed in the survey spectrum of pure NiMn$_2$O$_4$. The C 1s peak arises in the survey spectrum of NiMn$_2$O$_4$ due to addition of oxalic acid during the synthesis of NiMn$_2$O$_4$, while the C 1s peak in the ternary nanocomposite comes from both NiMn$_2$O$_4$ and rGO nanosheets [8]. The deconvoluted peaks of Mn 2p spectrum (Figure 6.5(ii)) centred at binding energies 637.6 and 642.2 eV are related to metallic Mn and oxides of Mn (Mn^{2+}/Mn^{3+}) [24]. The peaks

of Mn 2p spectrum at the binding energy positions of 642.2 and 653.9 eV with a separation of energy 11.7 eV are assigned to Mn 2p$_{3/2}$ and Mn 2p$_{1/2}$ electronic states, respectively. The Mn 2p spectrum also depict a significant shake-up peak in Figure 6.5(ii) around 644.6 eV related to the Coulomb interactions between the 3d orbital electrons of transition metal and the ligand O 2p [25]. The difference between the binding energy positions of two major peaks in Mn 2p spectrum and appearance of a significant shake-up peak imply the predominant existence of Mn^{2+} valence state [24]. However, from the Mn 2p spectrum it is difficult to distinguish contributions from all the possible valence states present in the sample owing to strong overlapping of all the photoemissions. The fitted spectrum of Ni 2p reveals the presence of two spin orbit doublets Ni 2p$_{1/2}$ at 873.3 eV and Ni 2p$_{3/2}$ at 854.7 eV in Figure 6.5 (iii). The deconvoluted peaks of Ni 2p at a binding energy of 854.4 eV and the satellite peak at 861.7 eV are due to presence of Ni^{2+} valence state, while the fitted peak at 856.2 eV can be attributed to Ni^{3+} oxidation state [26]. Moreover, the satellite peaks at 861.6 and 879.2 eV are ascribed to Ni 2p$_{3/2}$ and Ni 2p$_{1/2}$ edges. The deconvolution of C 1s spectrum in Figure 6.5 (iv) of ternary nanocomposite reveals two peaks at binding energies of 284.8 and 286.2 eV that correspond to C-C and C-O functional groups, respectively. The O 1s spectrum in Figure 6.5 (v) is deconvoluted into two peaks, one at 529.9 eV attributed to the metal-oxygen-metal (M-O-M) bond and another peak at 531.7 eV is due to presence of defects, surface contaminants and chemisorbed hydroxyl groups [27]. The two significant peaks in S 2p spectrum in Figure 6.5 (vi) indicate the presence of sulfur atoms from PEDOT and PSS. The deconvoluted peaks at 164 and 165.8 eV are related to S 2p$_{3/2}$ and S 2p$_{1/2}$ electronic configurations of thiophene ring in PEDOT, respectively [28]. Again, the peaks at binding energies of 168.2 and 169 eV are assigned to electronic states S 2p$_{3/2}$ of sulfonate (SO^{3-}) and S 2p$_{1/2}$ of sulfonic acid groups (SO$_3$H) in PSS, respectively [28].
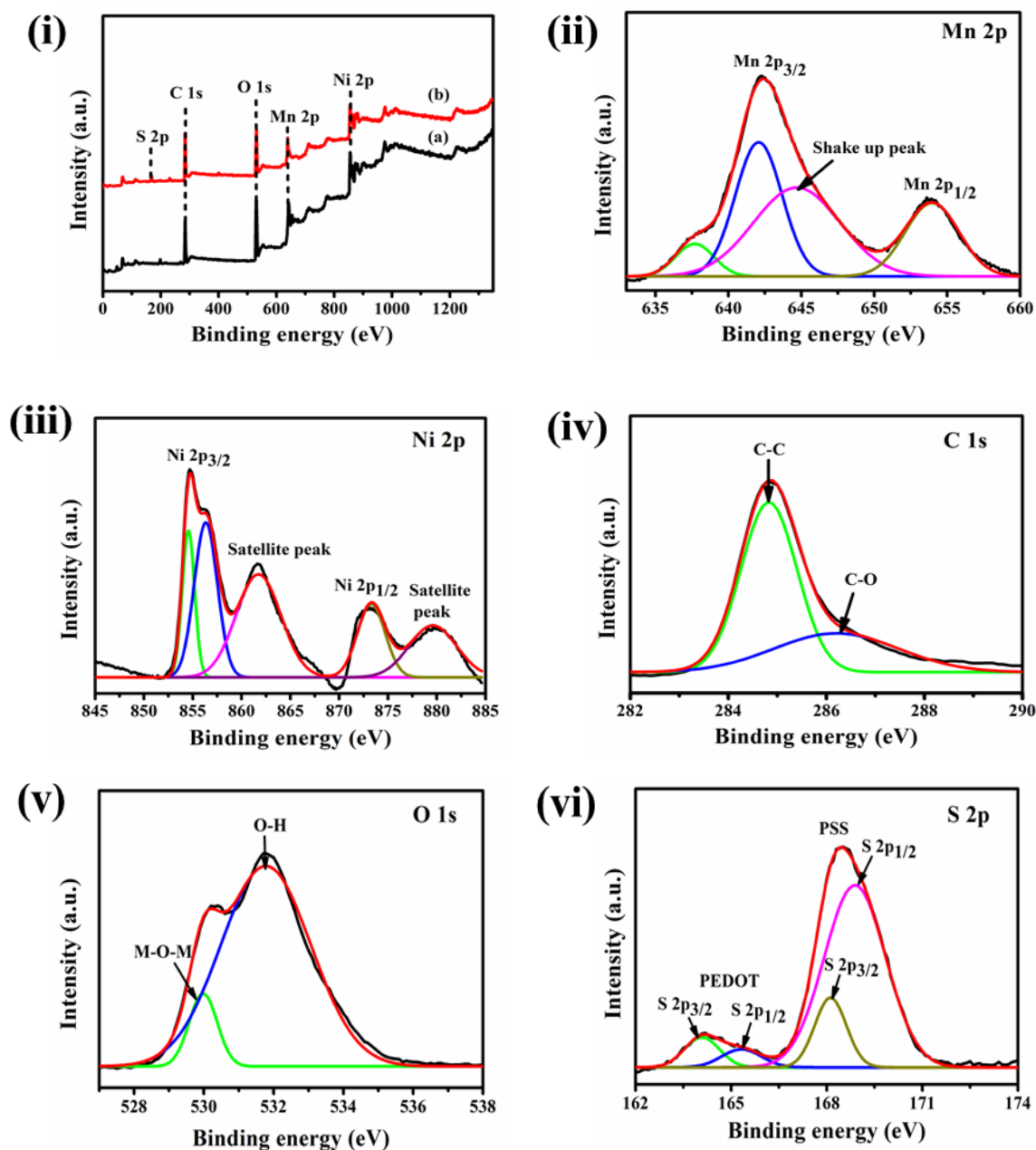
Figure 6.5: *(i) XPS survey spectra of (a) NiMn$_2$O$_4$ and (b) rGO/PEDOT:PSS/NiMn$_2$O$_4$ nanocomposite. High resolution XPS profile of (ii) Mn 2p, (iii) Ni 2p, (iv) C 1s, (v) O 1s and (vi) S 2p of rGO/PEDOT:PSS/NiMn$_2$O$_4$ nanocomposite.*

6.3.4 Nitrogen (N$_2$) adsorption-desorption analysis

The specific surface area and porosity of the as prepared samples have been investigated by nitrogen adsorption-desorption measurement at 77 K. Figures 6.6 (i), (ii) and (iii) display the nitrogen adsorption-desorption isotherms and the inset Figures represent corresponding BJH pore size distribution curves. Figure 6.6 (i) represents type II isotherm

of NiMn$_2$O$_4$ nanoparticles with a significant hysteresis loop within the P/P$_0$ range of 0.8-1.0, whereas Figures 6.6 (ii) and (iii) reveal type IV isotherms of PEDOT:PSS/NiMn$_2$O$_4$ and rGO/PEDOT:PSS/NiMn$_2$O$_4$ nanocomposites, respectively. Moreover, in Figures 6.6 (ii) and (iii), capillary condensation occurs at high relative pressures from 0.5 to 1.0, indicating presence of mesopores in the nanocomposites. The specific surface areas of the synthesized materials have been obtained by Brunauer-Emmett-Teller method using the data obtained from adsorption isotherm within the relative pressure range (P/P$_0$) of 0.05-0.3. The enhancement in BET surface area of rGO/PEDOT:PSS/NiMn$_2$O$_4$ nanocomposite (212 m^2 g^{-1}) compared to PEDOT:PSS/NiMn$_2$O$_4$ nanocomposite (92 m^2 g^{-1}) and NiMn$_2$O$_4$ (68 m^2 g^{-1}) is ascribed to the incorporation of rGO. The corresponding pore volumes of NiMn$_2$O$_4$, PEDOT:PSS/NiMn$_2$O$_4$ and rGO/PEDOT:PSS/NiMn$_2$O$_4$ nanocomposites are 0.16, 0.34 and 0.69 cm^3 g^{-1}, respectively. The insets of Figure 6.6 depict the distribution of pore size obtained from Barrett-Joyner-Halenda (BJH) method. From the pore size distribution curves, the average pore size of NiMn$_2$O$_4$ is found to be 4.5 nm. The average pore sizes of PEDOT:PSS/NiMn$_2$O$_4$ and rGO/PEDOT:PSS/NiMn$_2$O$_4$ nanocomposites are obtained as 5.6 nm and 8.5 nm, respectively. The wide pore size distributions of rGO/PEDOT:PSS/NiMn$_2$O$_4$ (4-35 nm) and PEDOT:PSS/NiMn$_2$O$_4$ nanocomposites (3-17 nm) ensure the existence of mesopores over the catalyst surface. Large area and mesoporous surface of the catalyst facilitate charge transport mechanism and penetration of the electrolyte into the electrode surface, which finally leads to the enhancement in electrochemical activities of the catalyst.
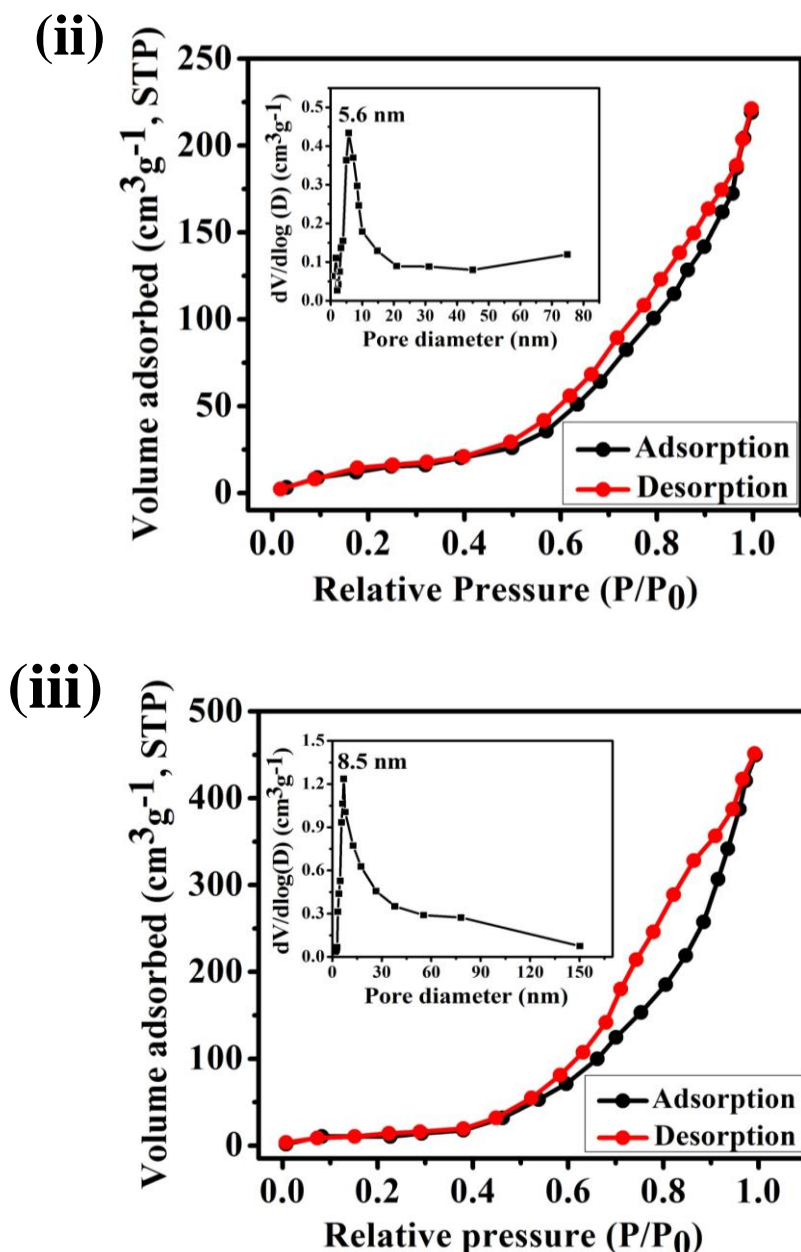
(ii)

(iii)
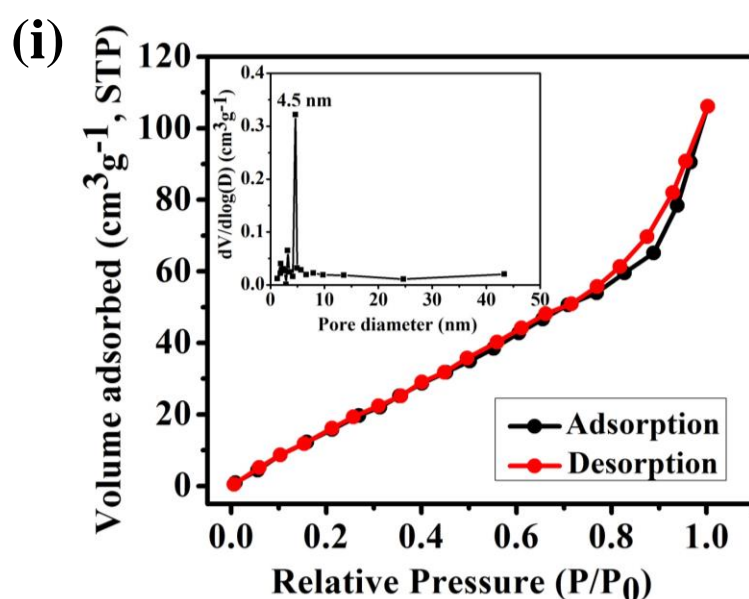
Figure 6.6: *N₂ adsorption-desorption isotherms of (i) NiMn₂O₄, (ii) PEDOT:PSS/NiMn₂O₄ and (iii) rGO/PEDOT:PSS/NiMn₂O₄ nanocomposites. Inset figures show pore size distribution.*

6.4 Electrochemical characterizations

6.4.1 Electrochemical activity of the modified electrodes

Figure 6.7 (i) depicts the CV profiles of NiMn₂O₄/ITO, PEDOT:PSS/NiMn₂O₄/ITO and rGO/PEDOT:PSS/NiMn₂O₄/ITO electrodes in presence of 0.5 M NaOH solution at a scan rate of 50 mV s⁻¹. The clearly visible oxidation and reduction peaks appear due to the

charge transfer mechanism in redox couples of Mn^{2+}/Mn^{3+} and Ni^{2+}/Ni^{3+} in $NiMn_2O_4$. These two pairs of redox couples act as two pairs of electroactive centres for redox mechanism. The appearance of redox peaks can be explained by the following reaction [29]:

$$NiMn_2O_4 + OH^- + H_2O \rightarrow NiOOH + 2MnOOH + e^- \qquad [6.1]$$
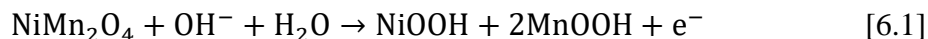
As shown in Figure 6.7 (i), rGO/PEDOT:PSS/NiMn₂O₄/ITO electrode exhibits much larger enclosed area and higher peak current density in comparison to the other two electrodes suggesting enhanced electroactivity of the electrode. rGO/PEDOT:PSS/NiMn₂O₄/ITO electrode exhibits less ΔEp (anodic peak to cathodic peak separation) value (87 mV) compared to PEDOT:PSS/NiMn₂O₄/ITO (111 mV) and NiMn₂O₄/ITO electrodes (137 mV).

6.4.1.1 Variation of anodic peak current (I_{pa}) and cathodic peak current (I_{pc}) vs. scan rate (v)
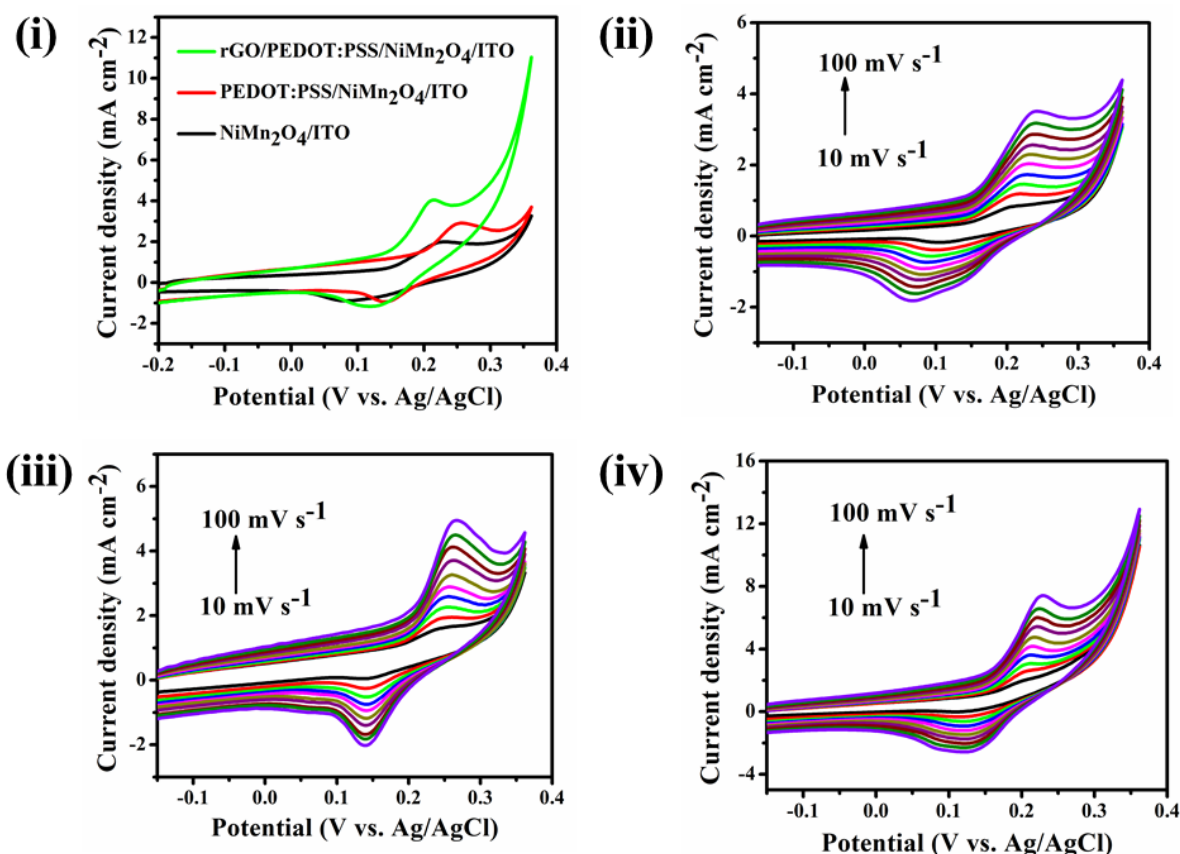

Figure 6.7: *Cyclic voltammograms of (i) NiMn₂O₄/ITO, PEDOT:PSS/NiMn₂O₄/ITO and rGO/PEDOT:PSS/NiMn₂O₄/ITO electrodes in 0.5 M NaOH solution at a scan rate of 50 mV s⁻¹. Cyclic voltammograms of (ii) NiMn₂O₄/ITO, (iii) PEDOT:PSS/NiMn₂O₄/ITO and*

(iv) rGO/PEDOT:PSS/NiMn₂O₄/ITO electrodes at different scan rates from 10 to 100 mV s⁻¹ in 0.5 M NaOH solution.

Figures 6.7 (ii), (iii) and (iv) are the CVs of as-prepared electrodes in 0.5 M NaOH electrolyte at different scan rates from 10 to 100 mV s⁻¹. On increase in scan rate, the forward peak shifts toward positive side, whereas the backward peak shifts toward negative side due to polarization at the electrode surface and also peak current density increases [23]. Moreover, the linear variations of ΔE_p of all the samples with change in scan rate imply quasi reversible mechanism [30].
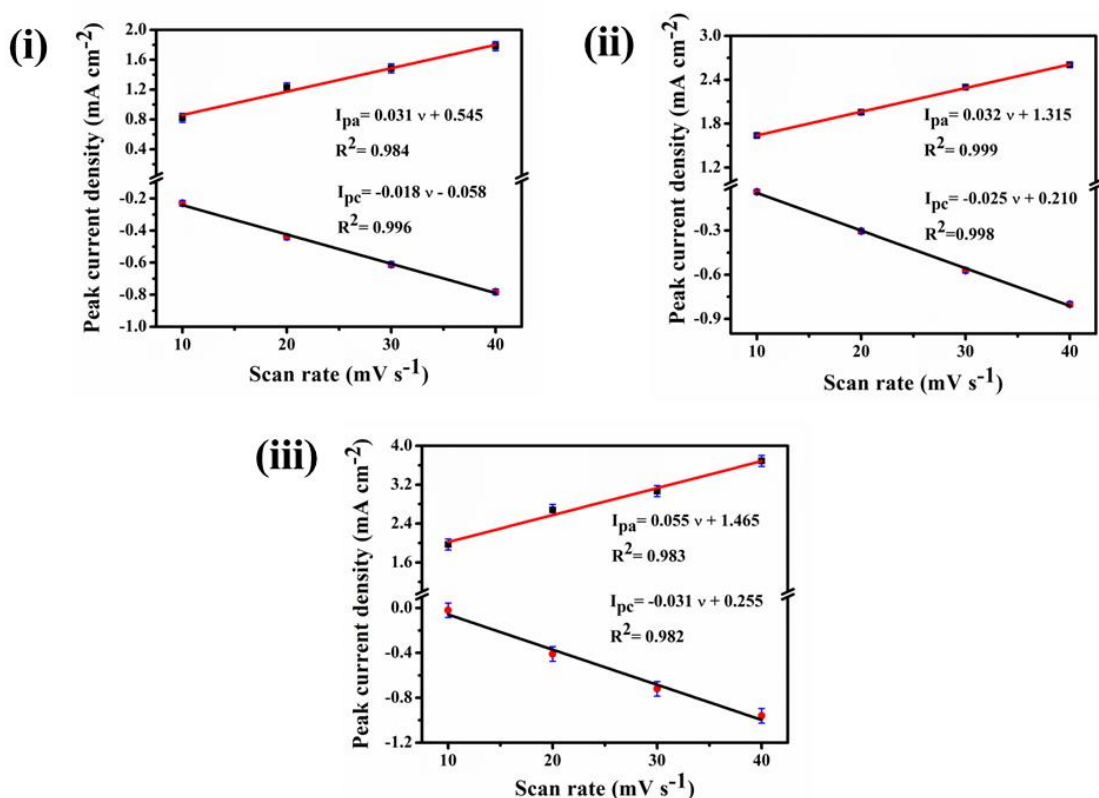

Figure 6.8: *The linear variation of anodic and cathodic peak current densities (I_p) vs. scan rate (v) (10-40 mV s⁻¹) of (i) NiMn₂O₄/ITO, (ii) PEDOT:PSS/NiMn₂O₄/ITO and (iii) rGO/PEDOT:PSS/NiMn₂O₄/ITO electrodes.*

The linear proportionality between peak current densities and lower value of scan rate (upto 40 mV s⁻¹), suggests electrochemical activity of the redox pairs (Figure 6.8). Surface concentrations (r*) of the redox pairs Mn^{2+}/Mn^{3+} and Ni^{2+}/Ni^{3+} over electrode surface are obtained from Brown-Anson model [31], as shown below:

$$I_p = \frac{n^2 F^2 r^* A v}{4RT}$$
[6.2]

Where I_p is the peak current density, n is the number of electrons transferred, F is the Faraday constant, A corresponds to electrode area, ν is the scan rate and R is the gas constant. The calculated values of concentrations of Mn^{2+}/Mn^{3+} and Ni^{2+}/Ni^{3} redox couples over the surface of $NiMn_2O_4/ITO$, $PEDOT:PSS/NiMn_2O_4/ITO$ and $rGO/PEDOT:PSS/NiMn_2O_4/ITO$ electrodes are 2.62×10^{-8}, 3.05×10^{-8} and 4.60×10^{-8} mol cm^{-2}, respectively. The surface concentrations of redox active couples over $rGO/PEDOT:PSS/NiMn_2O_4/ITO$ electrode is 1.5 folds and 1.75 folds larger as compared to $PEDOT:PSS/NiMn_2O_4/ITO$ and $NiMn_2O_4/ITO$ electrodes, respectively. The larger surface concentration over $rGO/PEDOT:PSS/NiMn_2O_4/ITO$ electrode is attributed to the large specific surface area of rGO having many electroactive sites.

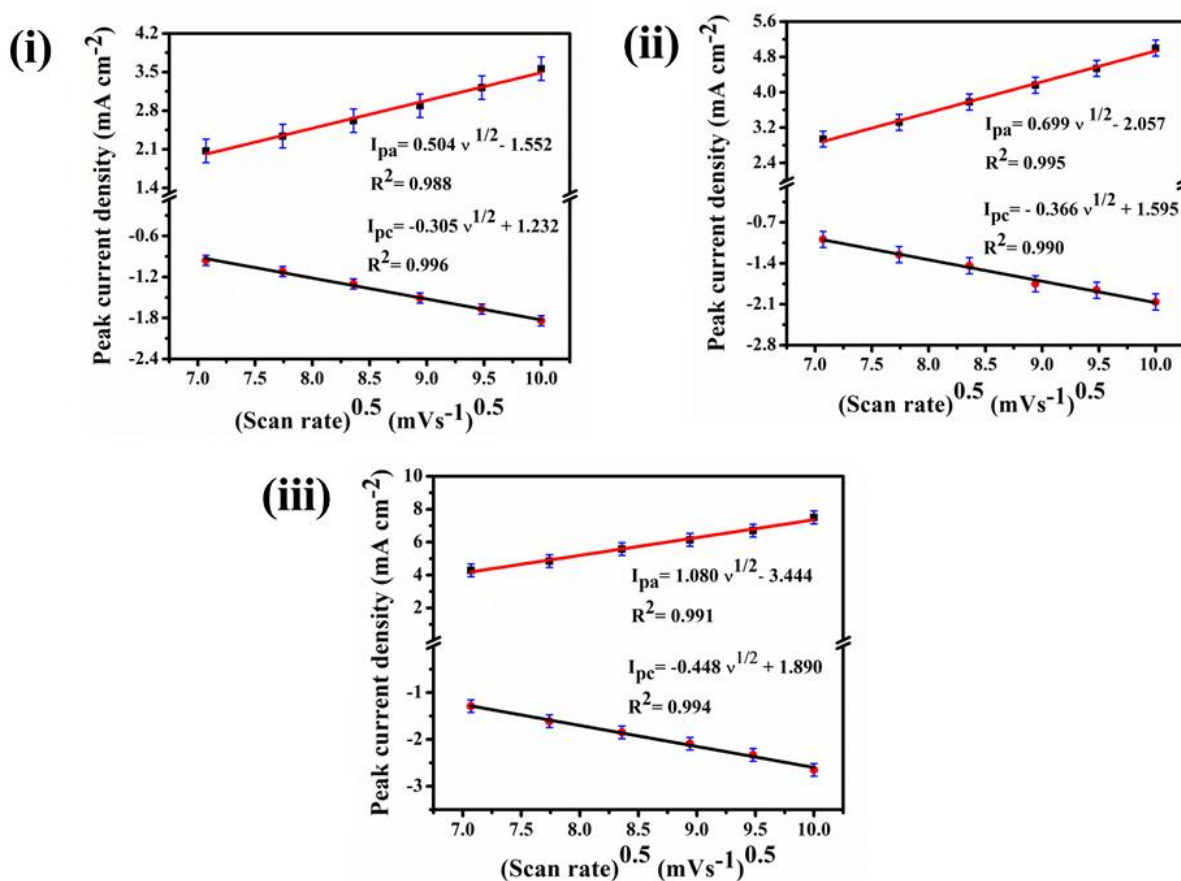***Figure 6.9:*** *Linear dependence of anodic and cathodic peak current densities on square root of scan rate (50-100 mV s⁻¹) for (i) NiMn₂O₄/ITO, (ii) PEDOT:PSS/NiMn₂O₄/ITO and (iii) rGO/PEDOT:PSS/NiMn₂O₄/ITO electrodes.*

The plots of peak current densities vs. square root of scan rate ($v^{1/2}$) of NiMn$_2$O$_4$/ITO, PEDOT:PSS/NiMn$_2$O$_4$/ITO and rGO/PEDOT:PSS/NiMn$_2$O$_4$/ITO electrodes in Figure 6.9 show a linear response at larger scan rates (50-100 mV s^{-1}), suggesting diffusion-controlled process followed by Faradaic reaction. The diffusion capability of hydroxyl ions is determined by the slope of linear plots of anodic peak currents (I_{pa}) against square roots of scan rate ($v^{1/2}$). The higher anodic slope value for rGO/PEDOT:PSS/NiMn$_2$O$_4$/ITO electrode (1.080) than that of PEDOT:PSS/NiMn$_2$O$_4$/ITO (0.699) and NiMn$_2$O$_4$/ITO (0.504) electrodes indicates faster diffusion capability of hydroxyl ions at the electrode, suggesting that large number of electroactive species formed on the electrode surface and also easy accessibility of Mn and Ni sites for hydroxyl ions in comparison to PEDOT:PSS/NiMn$_2$O$_4$/ITO and NiMn$_2$O$_4$/ITO electrodes.

6.4.1.2 Variation of anodic peak potential (E_{pa}) and cathodic peak potential (E_{pc}) vs. scan rate (v)
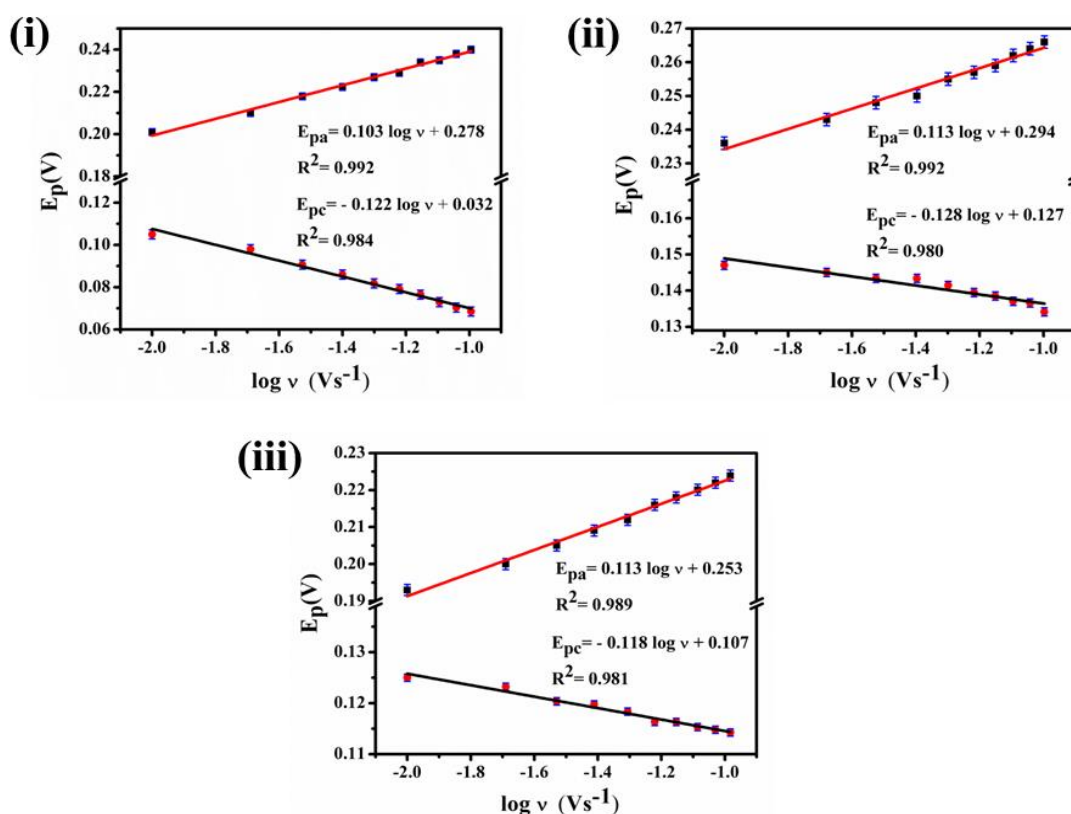

Figure 6.10: *Linear fitted plots of anodic and cathodic peak potentials (E_p) vs. logarithm of scan rate (log v) for (i) NiMn$_2$O$_4$/ITO, (ii) PEDOT:PSS/NiMn$_2$O$_4$/ITO and (iii) rGO/PEDOT:PSS/NiMn$_2$O$_4$/ITO electrodes.*

The shift in positions of anodic peak voltage (E_{pa}) and cathodic peak voltage (E_{pc}) of CV curves for the as prepared electrodes with logarithm of scan rate (log ν) has been investigated and plotted in Figure 6.10. According to Laviron's method [32], anodic electron transfer coefficient ($α_a$), cathodic electron transfer coefficient ($α_c$) and heterogeneous rate constant (k_s) are calculated using the slopes of anodic peak voltage (E_{pa}) and cathodic peak voltage (E_{pc}) vs. logarithm of scan rate (log ν), which are shown as:

$$E_{pc} = E^0 - 2.3RT\frac{\log υ}{αnF} \qquad [6.3]$$

$$E_{pa} = E^0 + 2.3RT\frac{\log υ}{(1-α)nF} \qquad [6.4]$$

$$\log k_s = α\log(1-α) + (1-α)\log α - \log\frac{RT}{nυF} - \frac{α(1-α)nF\Delta E_p}{2.3RT} \qquad [6.5]$$

Where, ΔE_p is the difference between positions of anodic and cathodic peak potentials and other terms have defined meanings. The values of $α_a$, $α_c$ and k_s from the anodic and cathodic slopes of the plot of E_{pa} and E_{pc} vs. log ν, have been listed in Table 6.1. The values of $α_a$ and $α_c$ are not same (as presented in Table 6.1), indicating that the rate limiting steps might be different for both oxidation and reduction process [33]. The higher value of k_s for rGO/PEDOT:PSS/NiMn$_2$O$_4$/ITO electrode suggests synergetic effects of redox active species (Mn^{2+}/Mn^{3+} and Ni^{2+}/Ni^{3+}) of NiMn$_2$O$_4$ nanoparticle and incorporated rGO nanosheets which enhance the kinetics of the electron transfer rate [11].
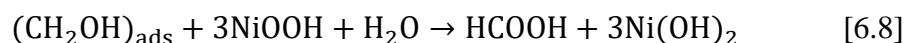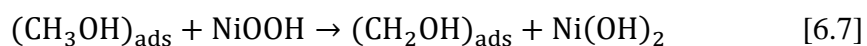
Table 6.1: *Calculated values of anodic electron transfer coefficient ($α_a$), cathodic electron transfer coefficient ($α_c$) and heterogeneous rate constant (k_s) of the modified electrodes.*

Electrodes	Anodic electron transfer coefficient ($α_a$)	Cathodic electron transfer coefficient ($α_c$)	Heterogeneous rate constant (k_s) (cm s^{-1})
NiMn$_2$O$_4$/ITO	0.43	0.48	0.075
PEDOT:PSS/NiMn$_2$O$_4$/ITO	0.48	0.46	0.081
rGO/PEDOT:PSS/NiMn$_2$O$_4$/ITO	0.48	0.50	0.150

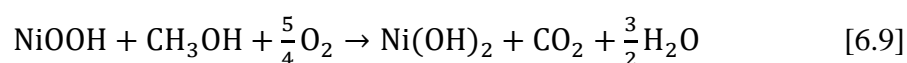## 6.4.2 Electrochemical activity of the electrodes toward methanol oxidation

Figure 6.11 (i) displays the comparative cyclic voltammograms of NiMn$_2$O$_4$/ITO, PEDOT:PSS/NiMn$_2$O$_4$/ITO and rGO/PEDOT:PSS/NiMn$_2$O$_4$/ITO electrodes in presence
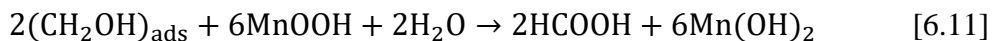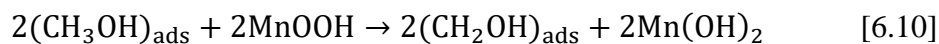
of 0.5 M methanol containing in 0.5 M NaOH at a scan rate of 50 mV s^{-1}. The voltammograms exhibit one well-defined anodic peak in forward direction. The electrocatalytic parameters which determine activity of the catalyst are (i) onset potential, the potential at which oxidation of alcohol just starts (a good electrocatalyst possess lower value of onset potential) and (ii) anodic peak current density indicates the maximum current generated by the electrocatalyst during methanol oxidation [34]. The onset potential at rGO/PEDOT:PSS/NiMn$_2$O$_4$/ITO electrode is less (0.21 V) in comparison to PEDOT:PSS/NiMn$_2$O$_4$/ITO (0.24 V) and NiMn$_2$O$_4$/ITO electrodes (0.26 V), while the anodic oxidation current density for rGO/PEDOT:PSS/NiMn$_2$O$_4$/ITO electrode is higher (70.4 mA cm^{-2}) than that of PEDOT:PSS/NiMn$_2$O$_4$/ITO (35.6 mA cm^{-2}) and NiMn$_2$O$_4$/ITO electrodes (15 mA cm^{-2}). Hence, the electrocatalytic activity of rGO/PEDOT:PSS/NiMn$_2$O$_4$/ITO electrode toward methanol oxidation is higher than that of PEDOT:PSS/NiMn$_2$O$_4$/ITO and NiMn$_2$O$_4$/ITO electrodes. The lower onset voltage of rGO/PEDOT:PSS/NiMn$_2$O$_4$/ITO electrode is due to synergetic effects of both redox active species of Ni and Mn, which boost the electrocatalytic activity of the electrode toward methanol oxidation. The reasons behind the excellent catalytic performance of rGO/PEDOT:PSS/NiMn$_2$O$_4$/ITO electrode are discussed below [8]: (i) the overall contributions of all the components present in the nanocomposite help in fast charge transport, (ii) the homogeneous distribution of NiMn$_2$O$_4$ nanoparticles (as shown in TEM image) within PEDOT:PSS matrix prevents aggregation of NiMn$_2$O$_4$ nanoparticles and thereby enhancing the surface area, (iii) the porous structure of rGO/PEDOT:PSS/NiMn$_2$O$_4$ nanocomposite enhances the migration and penetration of the ions into the electrode surface and (iv) incorporation of rGO nanosheets increases the electrical conductivity of the nanocomposite. Based on the proposal given by Fleishmann et al. [35], the oxidation of methanol on NiOOH is shown below:

$$(CH_3OH)_{sol.} \leftrightarrow (CH_3OH)_{ads} \qquad [6.6]$$

$$(CH_3OH)_{ads} + NiOOH \rightarrow (CH_2OH)_{ads} + Ni(OH)_2 \qquad [6.7]$$

$$(CH_2OH)_{ads} + 3NiOOH + H_2O \rightarrow HCOOH + 3Ni(OH)_2 \qquad [6.8]$$

The overall reaction can be written as [60]:

$$NiOOH + CH_3OH + \frac{5}{4}O_2 \rightarrow Ni(OH)_2 + CO_2 + \frac{3}{2}H_2O \qquad [6.9]$$

The possible methanol oxidation mechanism on MnOOH site is given as follows:

$$2(CH_3OH)_{ads} + 2MnOOH \rightarrow 2(CH_2OH)_{ads} + 2Mn(OH)_2 \qquad [6.10]$$

$$2(CH_2OH)_{ads} + 6MnOOH + 2H_2O \rightarrow 2HCOOH + 6Mn(OH)_2 \qquad [6.11]$$

The overall reaction can be written as [60]:

$$2MnOOH + 2CH_3OH + \frac{5}{2}O_2 \rightarrow 2Mn(OH)_2 + 2CO_2 + 3H_2O \qquad [6.12]$$
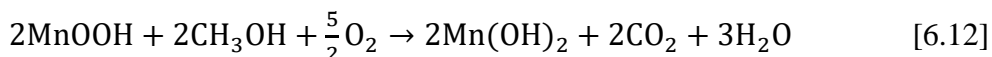
Initially, Ni and Mn in NiMn$_2$O$_4$ are oxidized into higher oxidation states (equation 6.1) and then the higher oxidation states of Ni and Mn oxidize methanol molecules and finally reduced back to lower oxidation states. The methanol oxidation mechanism is summarized below: in presence of hydroxyl (OH$^-$) ions (equation 6.1), NiMn$_2$O$_4$ is converted into NiOOH and MnOOH, which act as electroactive species in methanol oxidation. The methanol molecules easily get adsorbed on the electroactive sites of the electrode surface owing to large surface area and reactive edges of rGO nanosheets [36]. The oxidation of methanol molecules initiates through the cleavage of C-C and C-H bonds and then forming the carbonaceous intermediates. As reported in literature [37, 38], sufficient amount of OH species are required to oxidize these carbonaceous compounds, therefore the presence of oxyhydroxide species such as NiOOH and MnOOH facilitates the reaction conditions. The atomic oxygen used in methanol oxidation is obtained from splitting of water molecules [39]. According to water-gas shift reaction [40], the poisonous CO, by product of methanol oxidation is converted into CO$_2$. Regenerative redox mechanism is involved in water-gas shift reaction, where the water molecule is activated by removing hydrogen atom from water, which is followed by dissociation of the hydroxyl ions to oxygen atom [40]. Then CO is oxidized to CO$_2$ by reacting with atomic oxygen.

Considering the higher electrocatalytic performance of rGO/PEDOT:PSS/NiMn$_2$O$_4$/ITO electrode in comparison to PEDOT:PSS/NiMn$_2$O$_4$/ITO and NiMn$_2$O$_4$/ITO electrodes, further investigations on the electrocatalytic performance of rGO/PEDOT:PSS/NiMn$_2$O$_4$/ITO electrode have been done. Figure 6.11 (ii) reveals the CV profiles of rGO/PEDOT:PSS/NiMn$_2$O$_4$/ITO electrode with varying concentrations of methanol at a scan rate of 50 mV s^{-1} in 0.5 M NaOH. Linear increase in oxidation peak current density is observed with increase in concentrations of methanol. However, decrease in current density has been observed beyond 3 M concentration of methanol. This can be attributed to the blocking of electroactive sites present on the electrode

surface due to adsorption of excessive methanol molecules and thus resulting in decrease of oxidation peak current density at higher concentrations of methanol. The above results confirm the presence of available active sites on rGO/PEDOT:PSS/NiMn$_2$O$_4$/ITO electrode even at high methanol concentrations. Moreover, the oxidation potential remains constant upon increase in concentrations of methanol, indicating fewer amounts of carbonaceous intermediates is accumulated over the electrode causing easy mass transport.

Figure 6.11 (iii) shows the CV curves of rGO/PEDOT:PSS/NiMn$_2$O$_4$/ITO electrode in 0.5 M methanol solution at scan rates of 10, 30, 50, 70, 90, 110, 130 and 150 mV s^{-1}. The linear increase in current density with increase in square root of scan rate as shown in inset of Figure 6.11 (iii) indicates that the methanol oxidation at rGO/PEDOT:PSS/NiMn$_2$O$_4$/ITO electrode is diffusion controlled process.

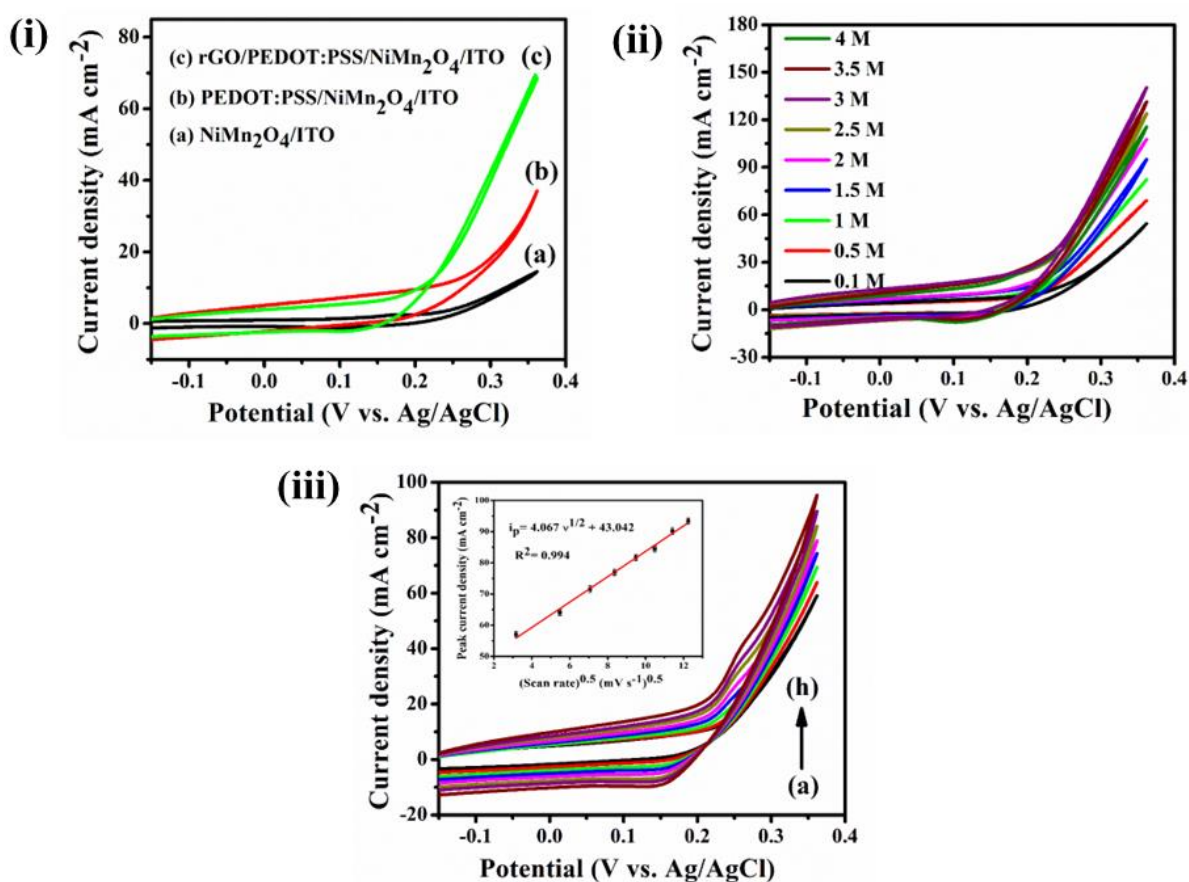*Figure 6.11: (i) Cyclic voltammograms of (a) NiMn$_2$O$_4$/ITO, (b) PEDOT:PSS/NiMn$_2$O$_4$/ITO and (c) rGO/PEDOT:PSS/NiMn$_2$O$_4$/ITO electrodes in presence of 0.5 M methanol containing in 0.5M NaOH as supporting electrolyte at a scan*

rate of 50 mV s⁻¹ (ii) Cyclic voltammograms of rGO/PEDOT:PSS/NiMn₂O₄/ITO electrode in presence of 0.1 M, 0.5 M, 1 M, 1.5 M, 2 M, 2.5 M, 3 M, 3.5 M and 4 M methanol at a scan rate of 50 mV s⁻¹; (iii) Cyclic voltammograms of rGO/PEDOT:PSS/NiMn₂O₄/ITO electrode in presence of 0.5 M methanol containing in 0.5 M NaOH at various scan rates (a) 10 mV s⁻¹, (b) 30 mV s⁻¹, (c) 50 mV s⁻¹,(d) 70 mV s⁻¹, (e) 90 mV s⁻¹, (f) 110 mV s⁻¹, (g) 130 mV s⁻¹ and (h) 150 mV s⁻¹ and inset figure shows corresponding plot between anodic peak current density and square root of scan rate.

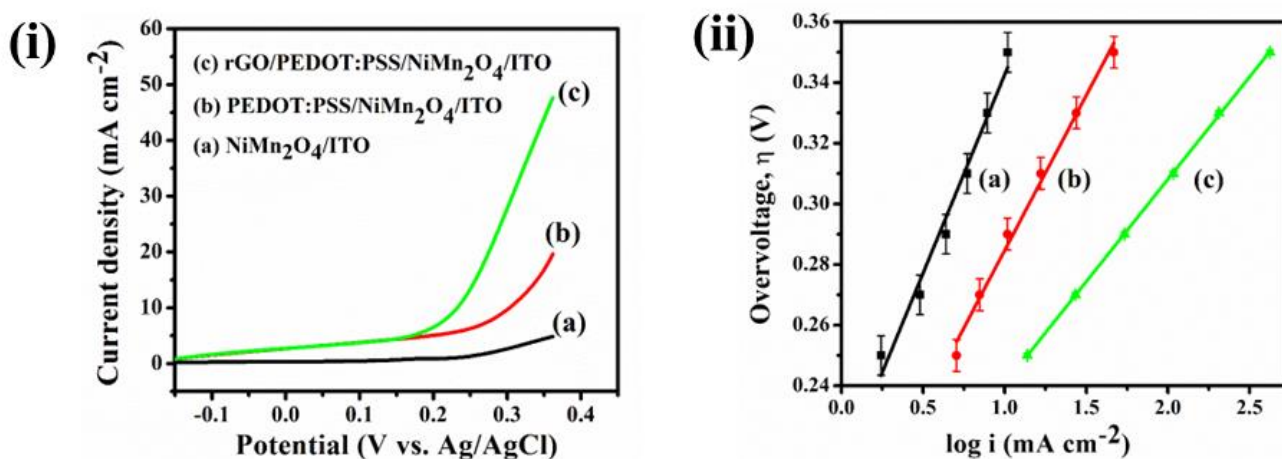### 6.4.3 Linear sweep voltammetry and Tafel analysis

Figure 6.12: *(i) Linear sweep voltammetry curves of (a) NiMn₂O₄/ITO, (b) PEDOT:PSS/NiMn₂O₄/ITO and (c) rGO/PEDOT:PSS/NiMn₂O₄/ITO electrodes in presence of 0.5 M methanol containing in 0.5 M NaOH at a scan rate of 1 mV s⁻¹. (ii) Tafel plots (η vs. log i) for the data obtained from rising part of LSV curves of (a) NiMn₂O₄/ITO, (b) PEDOT:PSS/NiMn₂O₄/ITO and (c) rGO/PEDOT:PSS/NiMn₂O₄/ITO electrodes.*

The kinetics of all the modified electrodes in methanol have been studied by the following kinetic parameters-Tafel slope (β), transfer coefficient (α) and exchange current density (i_0). The kinetic parameters can be obtained using the following equations [41]:

$$\eta = \beta \log i + C \qquad\qquad [6.13]$$

$$C = \beta \log i_0 \qquad\qquad [6.14]$$

$$\beta = \frac{2.303RT}{\alpha nF} \qquad\qquad [6.15]$$

Where η is the overpotential, i is the current density, C is the Tafel constant, i$_0$ is the exchange current density and the number of electrons exchanged is n. Figure 6.12 (ii) displays the Tafel diagrams (η vs. log i) plotted from the rising part of linear sweep voltammetry (LSV) curves in Figure 6.12 (i). The Tafel slope is lower at rGO/PEDOT:PSS/NiMn$_2$O$_4$/ITO electrode as compared to PEDOT:PSS/NiMn$_2$O$_4$/ITO and NiMn$_2$O$_4$/ITO electrodes indicating good electro activity of the electrode. Moreover, rGO/PEDOT:PSS/NiMn$_2$O$_4$/ITO electrode exhibits higher exchange current density in comparison to other two electrodes suggesting the fast electron transfer kinetics and stability of rGO/PEDOT:PSS/NiMn$_2$O$_4$/ITO electrode towards external causes.

Table 6.2: *Calculated values of Tafel slope, electron transfer coefficient and exchange current density from Tafel plot.*

Electrodes	Tafel slope (β) (mV dec^{-1})	Electron transfer coefficient (α)	Exchange current density (i$_o$) (mA cm^{-2})
NiMn$_2$O$_4$/ITO	130	0.45	4.74×10^{-4}
PEDOT:PSS/NiMn$_2$O$_4$/ITO	102	0.58	5.27×10^{-3}
rGO/PEDOT:PSS/NiMn$_2$O$_4$/ITO	67	0.88	5.61×10^{-2}

6.4.4 Chronoamperometry and Cyclic stability test

A good anode catalyst must exhibit high oxidation peak current density at less onset voltage, and maintains the uniform current for a longer duration. The stability of the electrodes has been studied by chronoamperometric (CA) measurements. Figure 6.13 (i) shows the chronoamperometric curves of all the electrodes in presence of 0.5 M methanol containing in 0.5 M NaOH. The generation of carbonaceous products during oxidation of methanol molecules causes poisoning and thus sudden current decay within first few seconds and then current becomes uniform throughout the period for all the electrodes [42]. As was obtained from CV data, rGO/PEDOT:PSS/NiMn$_2$O$_4$/ITO electrode exhibits higher oxidation current density than that of PEDOT:PSS/NiMn$_2$O$_4$/ITO and NiMn$_2$O$_4$/ITO electrodes. The values of steady current densities after 100 s of methanol oxidation have been found to be 5, 16.41 and 43 mA cm^{-2} at NiMn$_2$O$_4$/ITO, PEDOT:PSS/NiMn$_2$O$_4$/ITO and rGO/PEDOT:PSS/NiMn$_2$O$_4$/ITO electrodes, respectively. The values of current densities at 3600 s have been obtained as 2.58, 13.24 and 38 mA cm^{-2} at NiMn$_2$O$_4$/ITO, PEDOT:PSS/NiMn$_2$O$_4$/ITO and rGO/PEDOT:PSS/NiMn$_2$O$_4$/ITO electrodes, respectively. The higher current retention

factor of rGO/PEDOT:PSS/NiMn$_2$O$_4$/ITO electrode (65.2%) than that of PEDOT:PSS/NiMn$_2$O$_4$/ITO (45.8%) and NiMn$_2$O$_4$/ITO (24.1%) electrodes indicates better stability of rGO/PEDOT:PSS/NiMn$_2$O$_4$/ITO electrode as compared to the other two.
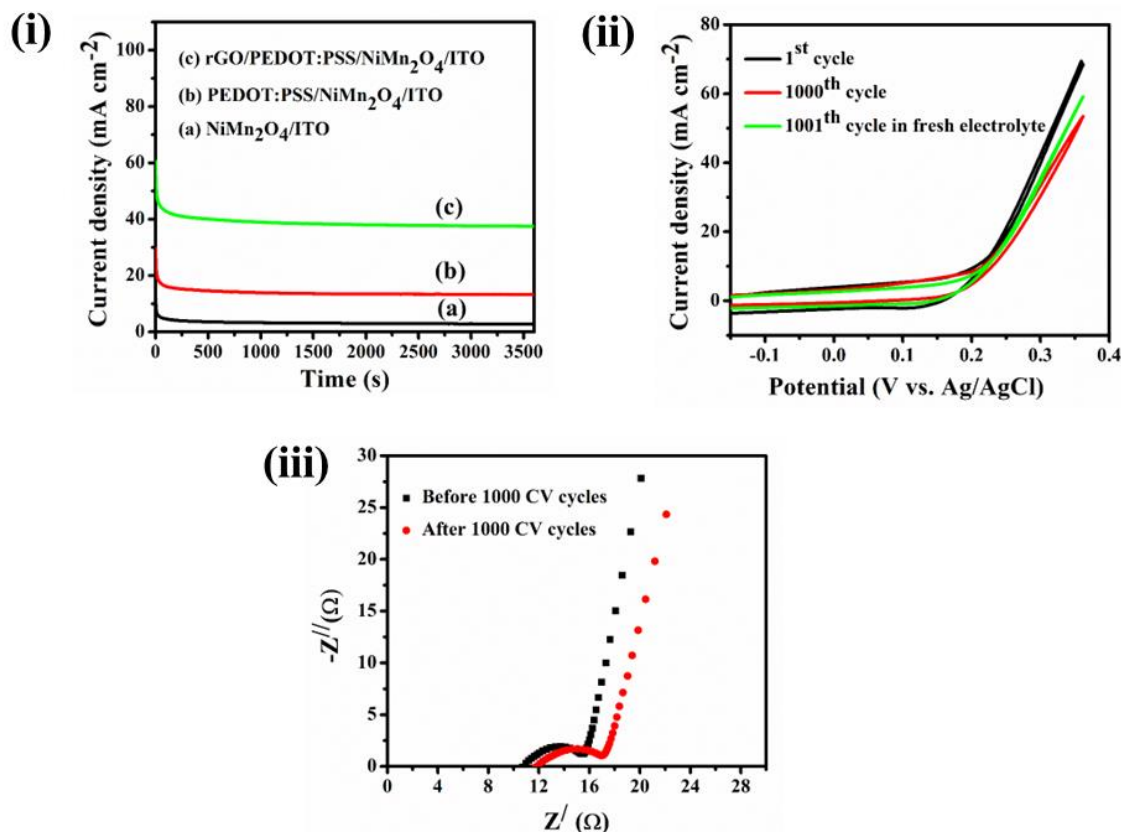

Figure 6.13: (i) Chronoamperometric curves of (a) NiMn$_2$O$_4$/ITO, (b) PEDOT:PSS/NiMn$_2$O$_4$/ITO and (c) rGO/PEDOT:PSS/NiMn$_2$O$_4$/ITO electrodes in 0.5 M methanol solution containing in 0.5 M NaOH at an applied potential 0.21 V; (ii) Cyclic stability of rGO/PEDOT:PSS/NiMn$_2$O$_4$/ITO electrode for 1000 CV cycles in 0.5 methanol solution containing in 0.5 M NaOH at a scan rate of 50 mV s^{-1}. (iii) EIS curves of rGO/PEDOT:PSS/NiMn$_2$O$_4$/ITO electrode in 0.5 M NaOH solution in presence of 0.5 M methanol before and after 1000 CV cycles.

The cyclic stability performance of rGO/PEDOT:PSS/NiMn$_2$O$_4$/ITO electrode has been investigated in presence of 0.5 M methanol containing in 0.5 M NaOH at a scan rate of 50 mV s^{-1} for 1000 CV cycles. As shown in Figure 6.13 (ii), rGO/PEDOT:PSS/NiMn$_2$O$_4$/ITO electrode exhibits decrease in current density after 1000 CV cycles and maintains 77.4% current retention of 1st cycle. The oxidation current

density drops on increase in number of cycles on account of blockage of surface active redox sites present in the electrode by the intermediates generated during methanol oxidation. Moreover, consumption of methanol also facilitates decrease in current density. However, the current retention becomes 85.2% of initial cycle after replacing the electrolyte with fresh one.

6.4.5 Electrochemical impedance spectroscopy measurements after cyclic stability test

 Figure 6.13 (iii) depicts the Nyquist plot of rGO/PEDOT:PSS/NiMn$_2$O$_4$/ITO electrode recorded before and after 1000 CV cycles in presence of 0.5 M methanol solution containing in 0.5 M NaOH. In Nyquist plots, the semicircle at high frequency side and the straight line at low frequency side are related to charge transfer resistance (R_{ct}) and capacitive behaviour, respectively. The charge transfer resistance of rGO/PEDOT:PSS/NiMn$_2$O$_4$/ITO electrode slightly increases from 4.2 Ω to 5.15 Ω and also the Warburg impedance line inclines towards lower angle side after cyclic stability test for 1000 CV cycles indicating good stability of the electrode. The formation of intermediates during methanol oxidation and change in diffusion path length lead to the increase in charge transfer resistance and inclination of Warburg impedance line after stability test.

6.4.6 Characterizations after cyclic stability test

To study the morphology, structure and composition of the electrode after stability test for 1000 CV cycles TEM, XRD and XPS measurements have been done. TEM images (Figures 6.14 (i) and (ii)) show slight agglomeration (as shown in red circles) of NiMn$_2$O$_4$ nanoparticles and increase in diameter that lies within the range of 50-60 nm. The XRD patterns of rGO/PEDOT:PSS/NiMn$_2$O$_4$/ITO electrode have been recorded after cyclic stability test for 1000 CV cycles in 0.5 M methanol solutions to check the structural stability of the electrode. Figure 6.14 (iii) shows that the intensities of characteristic peaks of the electrode decrease slightly indicating decrease in crystallinity of the nanocomposite after stability test. However, no new phase has been observed even after prolonged cycling. The sharp peaks of ITO glasses at 21°, 30.5°, 35.4°, 45.7°, 51° and 60.6° correspond to (211), (222), (400), (431), (440) and (622) planes, respectively.
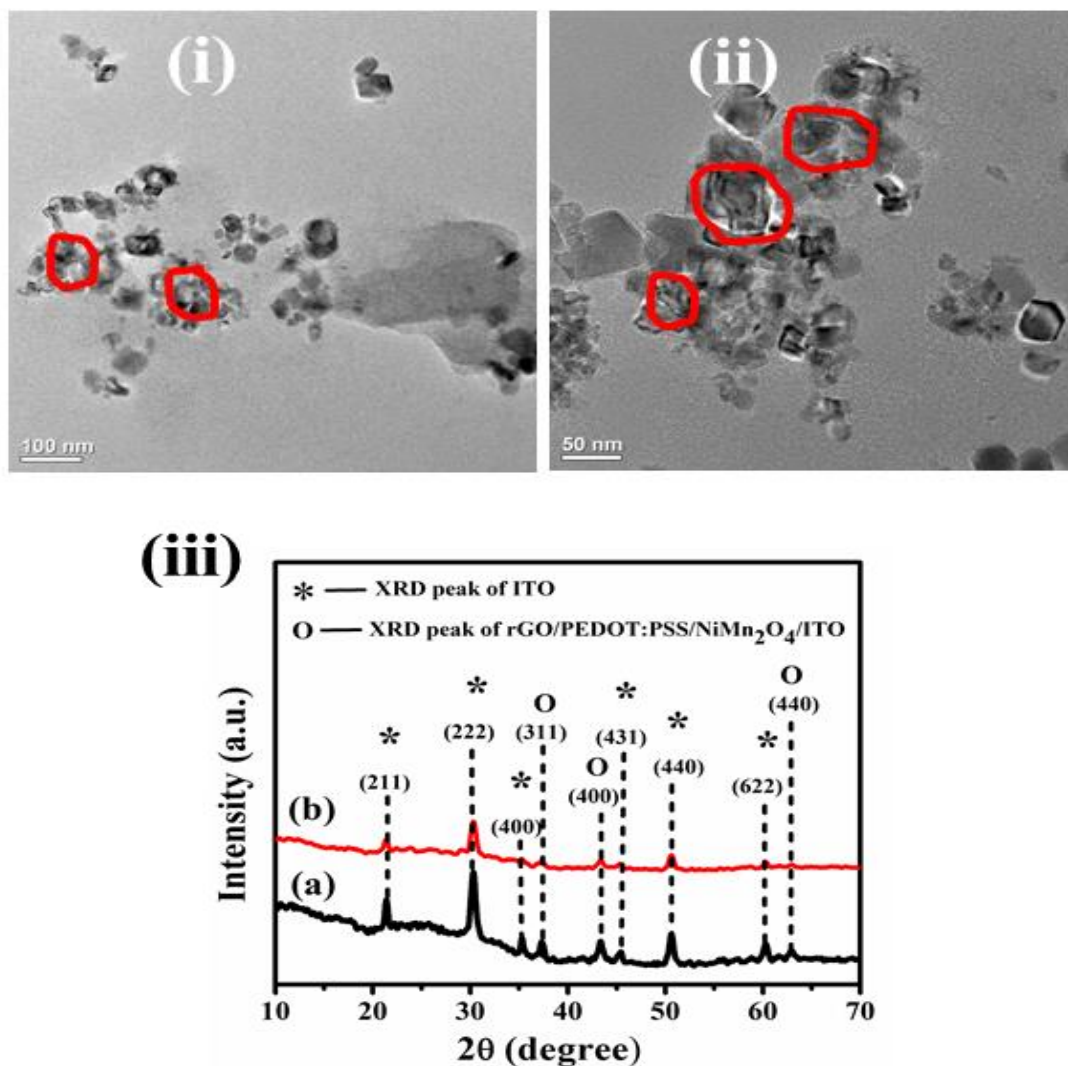
Figure 6.14: *TEM micrographs of rGO/PEDOT:PSS/NiMn$_2$O$_4$ nanocomposite after 1000 CV cycles in 0.5 M methanol containing solution at resolutions of (i) 100 nm and (ii) 50 nm, (iii) XRD patterns of (a) rGO/PEDOT:PSS/NiMn$_2$O$_4$ nanocomposite and (b) rGO/PEDOT:PSS/NiMn$_2$O$_4$/ITO electrode after 1000 CV cycles in 0.5 M methanol containing solution.*

The XPS measurements of rGO/PEDOT:PSS/NiMn$_2$O$_4$ nanocomposite before stability test and rGO/PEDOT:PSS/NiMn$_2$O$_4$/ITO electrode after stability test for 1000 CV cycles in 0.5 M methanol containing solution have been plotted in Figure 6.15 (i)-(vi). The appearance of C 1s, O 1s, Mn 2p, Ni 2p and S 2p peaks in the survey spectrum (Figure 6.15 (i)) of rGO/PEDOT:PSS/NiMn$_2$O$_4$/ITO electrode confirms the presence of these elements in the electrode even after 1000 CV cycles. However, a small intense peak appears at 1075 eV attributing to Na 1s peak indicating the adsorption of Na$^+$ ions over

the surface of electrode from electrolyte due to continuous CV cycling. The peaks at 33.1, 501.2 and 690.6 eV correspond to In 4d, Sn 3d and In 3p bands of ITO, respectively [43]. From Figure 6.15 (ii), it has been observed that the intensities of Mn 2p$_{3/2}$ and Mn 2p$_{1/2}$ decrease after stability test due to continuous transition between the electroactive media Mn(OH)$_2$ and MnOOH causing consumption of Mn species during oxidation of methanol. As shown in Figure 6.15 (iii), the intensities of peaks at 854.4 eV related to Ni^{2+} oxidation state and at 856.2 eV corresponding to Ni^{3+} state decrease after 1000 CV cycles. Moreover, the peak at 873.3 eV corresponding to Ni 2p$_{1/2}$ state diminishes and also the intensity of satellite peak at 879.2 eV decreases considerably. Ni(OH)$_2$ and NiOOH formed during electrochemical reaction of rGO/PEDOT:PSS/NiMn$_2$O$_4$/ITO electrode, act as electroactive media for methanol oxidation. Hence significant amount of Ni species are consumed during continuous 1000 CV cycles that causing decrease in intensities of characteristic XPS peaks of Ni 2p spectrum. In C 1s spectrum (Figure 6.15 (iv)), the decrease in intensity of deconvoluted peak at 284.8 eV attributing to C-C bond indicates the consumption of carbon content in rGO/PEDOT:PSS/NiMn$_2$O$_4$/ITO electrode during 1000 CV cycles and also a satellite peak arises at 291.8 eV. As shown in Figure 6.15 (v), the intensity of deconvoluted peak of O 1s spectrum at 531.1 eV related to M-O-M group decreases slightly owing to the consumption of manganese and nickel ions during methanol oxidation and a broad peak appears at 535.1 eV associated with sodium Auger peak (NaKLL) implying that considerable amount of Na$^+$ ions are present over the electrode surface. In Figure 6.15 (vi), disappearance of S 2p$_{3/2}$ and S 2p$_{1/2}$ electronic states of PEDOT in S 2p spectrum indicates degradation of PEDOT after stability test.
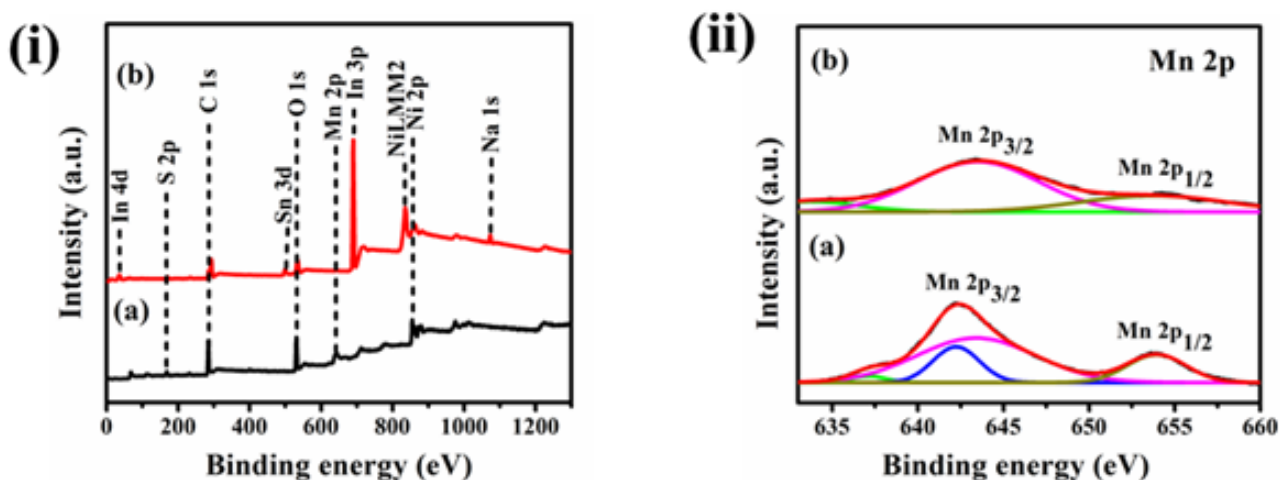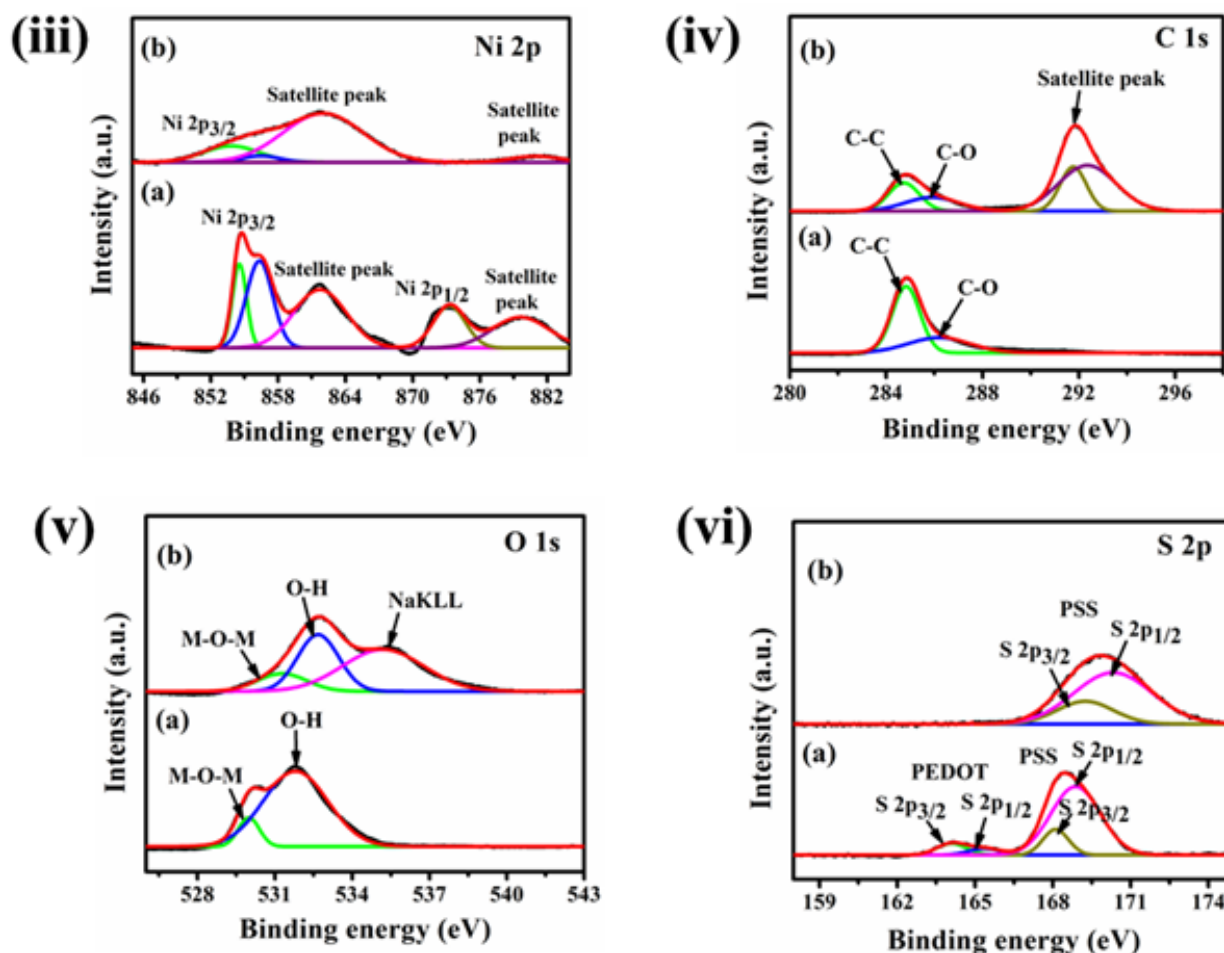
Figure 6.15: (i) Survey spectra of (a) rGO/PEDOT:PSS/NiMn₂O₄ nanocomposite (b) rGO/PEDOT:PSS/NiMn₂O₄/ITO electrode after 1000 CV cycles, Core-level XPS spectra of (ii) Mn 2p, (iii) Ni 2p, (iv) C 1s, (v) O 1s and (vi) S 2p regions of (a) rGO/PEDOT:PSS/NiMn₂O₄ nanocomposite (b) rGO/PEDOT:PSS/NiMn₂O₄/ITO electrode after 1000 CV cycles in 0.5 M methanol containing in 0.5 M NaOH solution.

6.5 Summary

In this chapter, a ternary nanocomposite has been synthesized by compositing $NiMn_2O_4$, PEDOT:PSS and rGO nanosheets via *in situ* polymerization method. rGO/PEDOT:PSS/$NiMn_2O_4$ nanocomposite exhibits porous nanostructures with BET specific surface area of 212 m^2 g^{-1} and pore volume of 0.69 cm^3 g^{-1}. rGO/PEDOT:PSS/$NiMn_2O_4$/ITO electrode exhibits good electrocatalytic activity with an oxidation peak current density of 70.4 mA cm^{-2} at an onset voltage of 0.21 V and 65%

current retention for 1 h in presence of 0.5 methanol containing in 0.5 NaOH solution. Tafel plots show comparatively better electron transfer kinetics for rGO/PEDOT:PSS/NiMn$_2$O$_4$/ITO electrode than that of PEDOT:PSS/NiMn$_2$O$_4$/ITO and NiMn$_2$O$_4$/ITO electrodes with high exchange current density (i_0) of $5.61 \times 1\ 0^{-2}$ mA cm^{-2} in 0.5 M methanol solution. The main role of redox active species (Mn^{2+}/Mn^{3+} and Ni^{2+}/Ni^{3+}) present in NiMn$_2$O$_4$ nanoparticles in methanol oxidation has been discussed by a given mechanism in the chapter. The TEM micrographs show slight aggregation of NiMn$_2$O$_4$ nanoparticles after stability test for 1000 CV cycles. The decrease in crystallinity of characteristic XRD peaks of rGO/PEDOT:PSS/NiMn$_2$O$_4$/ITO electrode has been observed after stability test. The XPS survey spectrum of rGO/PEDOT:PSS/NiMn$_2$O$_4$/ITO electrode confirms the presence of Mn 2p, Ni 2p, C 1s, O 1s and S 2p peaks even after 1000 CV cycles. However, the intensity of deconvoluted peaks of Mn 2p and Ni 2p decreases due to consumption of Mn and Ni species during methanol oxidation. The decrease in intensity of XPS peak at a binding energy of 284.8 eV in C 1s spectra related to C-C bond indicates the consumption of carbon content due to continuous CV cycles. Moreover, the XPS peaks corresponding to S 2p$_{3/2}$ and S 2p$_{1/2}$ electronic states of PEDOT disappear in S 2p spectrum suggesting degradation of PEDOT after stability test. A small intense peak observed at 1075 eV in the survey spectrum of rGO/PEDOT:PSS/NiMn$_2$O$_4$/ITO electrode corresponding to Na 1s band confirms the accumulation of Na$^+$ ions over the electrode surface from electrolyte during continuous CV cycles. The good electrocatalytic performance of rGO/PEDOT:PSS/NiMn$_2$O$_4$/ITO electrode toward methanol oxidation is due to synergetic effects of rich binary redox active sites of Ni and Mn species, high electrical conductivity and high surface area of rGO nanosheets, uniform distribution of NiMn$_2$O$_4$ nanoparticles within polymer matrix without any agglomeration and the porous structure of the ternary nanocomposite.

6.6 References

[1] Ding, R., Qi, L., Jia, M. and Wang, H. Porous NiCo$_2$O$_4$ nanostructures as bi-functional electrocatalysts for CH$_3$OH oxidation reaction and H$_2$O$_2$ reduction reaction. *Electrochimica Acta*, 113:290-301, 2013.

[2] Wang, Z., Zhu, Z., Zhang, C., Xu, C. and Chen, C. Facile synthesis of reduced graphene oxide/NiMn$_2$O$_4$ nanorods hybrid materials for high-performance supercapacitors. *Electrochimica Acta*, 230:438-444, 2017.

[3] Wei, H., Wang, J., Yu, L., Zhang, Y., Hou, D. and Li, T. Facile synthesis of NiMn$_2$O$_4$ nanosheet arrays grown on nickel foam as novel electrode materials for high-performance supercapacitors. *Ceramics International*, 42(13):14963-14969, 2016.

[4] Ko, T.H., Devarayan, K., Seo, M.K., Kim, H.Y. and Kim, B.S. Facile synthesis of core/shell-like NiCo$_2$O$_4$-decorated MWCNTs and its excellent electrocatalytic activity for methanol oxidation. *Scientific reports*, 6(1):1-9, 2016.

[5] Zhang, G., Controlled growth of NiCo$_2$O$_4$ nanorods and ultrathin nanosheets on carbon nanofibers for high-performance supercapacitors. *Scientific reports*, 3(1):1-6, 2013.

[6] Saranya, P.E. and Selladurai, S. Efficient electrochemical performance of ZnMn$_2$O$_4$ nanoparticles with rGO nanosheets for electrodes in supercapacitor applications. *Journal of Materials Science: Materials in Electronics*, 29(4):3326-3339, 2018.

[7] Umeshbabu, E. and Rao, G.R. NiCo$_2$O$_4$ hexagonal nanoplates anchored on reduced graphene oxide sheets with enhanced electrocatalytic activity and stability for methanol and water oxidation. *Electrochimica Acta*, 213:717-729, 2016.

[8] Sahoo, S., Zhang, S. and Shim, J.J. Porous ternary high performance supercapacitor electrode based on reduced graphene oxide, NiMn$_2$O$_4$, and polyaniline. *Electrochimica Acta*, 216:386-396, 2016.

[9] Ahamed, M.I., Asiri, A.M. and AlAmry, K.A. Biocompatible mediated bioanode prepared by using poly (3, 4-ethylene dioxythiophene) poly (styrene sulfonate)(PEDOT: PSS) and sulfonated graphene oxide integrated enzyme for biofuel cells applications. *Materials Science for Energy Technologies*, 1(1):63-69, 2018.

[10] Salarizadeh, P., Askari, M.B., Beheshti-Marnani, A., Rozati, S.M., Rohani, T., Askari, N., Salarizadeh, N. and Mohammadi, S.Z. Synthesis and characterization of $(Co, Fe, Ni)_9S_8$ nanocomposite supported on reduced graphene oxide as an efficient and stable electrocatalyst for methanol electrooxidation toward DMFC. *Journal of Materials Science: Materials in Electronics*, 30(4):3521-3529, 2019.

[11] Askari, M.B. and Salarizadeh, P. Superior catalytic performance of $NiCo_2O_4$ nanorods loaded rGO towards methanol electro-oxidation and hydrogen evolution reaction. *Journal of Molecular Liquids*, 291:111306, 2019.

[12] Wu, Z.S., Zhou, G., Yin, L.C., Ren, W., Li, F. and Cheng, H.M. Graphene/metal oxide composite electrode materials for energy storage. *Nano Energy*, 1(1):107-131, 2012.

[13] Abulizi, A., Yang, G.H. and Zhu, J.J. One-step simple sonochemical fabrication and photocatalytic properties of Cu_2O-rGO composites. *Ultrasonics sonochemistry*, 21(1):129-135, 2014.

[14] Du, F.P., Cao, N.N., Zhang, Y.F., Fu, P., Wu, Y.G., Lin, Z.D., Shi, R., Amini, A. and Cheng, C. PEDOT: PSS/graphene quantum dots films with enhanced thermoelectric properties via strong interfacial interaction and phase separation. *Scientific reports*, 8(1):1-12, 2018.

[15] Larbi, T., Labidi, A. and Amlouk, M. Ethanol sensing properties and photocatalytic degradation of methylene blue by Mn_3O_4, $NiMn_2O_4$ and alloys of Ni-manganates thin films. *Journal of Alloys and Compounds*, 686:168-175, 2016.

[16] Larbi, T., Amara, A., Ouni, B., Inoubli, A., Karyaoui, M., Yumak, A.Y.Ş.E., Saadallah, F., Boubaker, K. and Amlouk, M. Physical investigations on $NiMn_2O_4$ sprayed magnetic spinel for sensitivity applications. *Journal of Magnetism and Magnetic Materials*, 387: 139-146, 2015.

[17] Ram, J., Singh, R.G., Singh, F., Kumar, V., Chauhan, V., Gupta, R., Kumar, U., Yadav, B.C. and Kumar, R. Development of WO_3-PEDOT: PSS hybrid nanocomposites based devices for liquefied petroleum gas (LPG) sensor. *Journal of Materials Science: Materials in Electronics*, 30(14):13593-13603, 2019.

[18] Xu, B., Gopalan, S.A., Gopalan, A.I., Muthuchamy, N., Lee, K.P., Lee, J.S., Jiang, Y., Lee, S.W., Kim, S.W., Kim, J.S. and Jeong, H.M. Functional solid additive modified PEDOT: PSS as an anode buffer layer for enhanced

photovoltaic performance and stability in polymer solar cells. *Scientific Reports*, 7(1):1-13, 2017.

[19] Nguyen, T.P. and De Vos, S.A. An investigation into the effect of chemical and thermal treatments on the structural changes of poly(3,4-ethylenedioxythiophene)/polystyrenesulfonate and consequences on its use on indium tin oxide substrates. *Applied Surface Science*, 221(1-4):330-339, 2004.

[20] Wilamowska, M., Kujawa, M., Michalska, M., Lipińska, L. and Lisowska-Oleksiak, A. Electroactive polymer/graphene oxide nanostructured composites; evidence for direct chemical interactions between PEDOT and GOx. *Synthetic Metals*, 220:334-346, 2016.

[21] Ferrari, A.C. and Basko, D.M. Raman spectroscopy as a versatile tool for studying the properties of graphene. *Nature nanotechnology*, 8(4):235-246, 2013.

[22] Ranjan, P., Agrawal, S., Sinha, A., Rao, T.R., Balakrishnan, J. and Thakur, A.D. A low-cost non-explosive synthesis of graphene oxide for scalable applications. *Scientific Reports*, 8:12007, 2018.

[23] Yu, M., Chen, J., Liu, J., Li, S., Ma, Y., Zhang, J. and An, J. Mesoporous NiCo$_2$O$_4$ nanoneedles grown on 3D graphene-nickel foam for supercapacitor and methanol electro-oxidation. *Electrochimica Acta*, 151:99-108, 2015.

[24] Maiti, S., Pramanik, A., Dhawa, T., Sreemany, M. and Mahanty, S. Bi-metal organic framework derived nickel manganese oxide spinel for lithium-ion battery anode. *Materials Science and Engineering: B*, 229:27-36, 2018.

[25] Ngo, Y.L.T., Sui, L., Ahn, W., Chung, J.S. and Hur, S.H. NiMn$_2$O$_4$ spinel binary nanostructure decorated on three-dimensional reduced graphene oxide hydrogel for bifunctional materials in non-enzymatic glucose sensor. *Nanoscale*, 9(48):19318-19327, 2017.

[26] He, X., Yin, F., Li, Y., Wang, H., Chen, J., Wang, Y. and Chen, B. NiMnO$_3$/NiMn$_2$O$_4$ oxides synthesized via the aid of pollen: ilmenite/spinel hybrid nanoparticles for highly efficient bifunctional oxygen electrocatalysis. *ACS applied materials & interfaces*, 8(40):26740-26757, 2016.

[27] Bhagwan, J., Rani, S., Sivasankaran, V., Yadav, K.L. and Sharma, Y. Improved energy storage, magnetic and electrical properties of aligned, mesoporous and high aspect ratio nanofibers of spinel-NiMn$_2$O$_4$. *Applied Surface Science*, 426:913-923, 2017.

[28] Lee, S.B., Lee, S.M., Park, N.I., Lee, S. and Chung, D.W. Preparation and characterization of conducting polymer nanocomposite with partially reduced graphene oxide. *Synthetic Metals*, 201:61-66, 2015.

[29] Wu, J.B., Li, Z.G., Huang, X.H. and Lin, Y. Porous Co_3O_4/NiO core/shell nanowire array with enhanced catalytic activity for methanol electro-oxidation. *Journal of power sources*, 224:1-5, 2013.

[30] Elgrishi, N., Rountree, K.J., McCarthy, B.D., Rountree, E.S., Eisenhart, T.T. and Dempsey, J.L. A practical beginner's guide to cyclic voltammetry. *Journal of chemical education*, *95*(2):197-206, 2018.

[31] Pickup, P.G., Kuo, K.N. and Murray, R.W., Electrodeposition of metal particles and films by a reducing redox polymer. *Journal of the Electrochemical Society*, 130(11):2205, 1983.

[32] Laviron, E.J.J. General expression of the linear potential sweep voltammogram in the case of diffusionless electrochemical systems. *Journal of Electroanalytical Chemistry and Interfacial Electrochemistry*, 101(1):19-28, 1979.

[33] Luo, H., Shi, Z., Li, N., Gu, Z. and Zhuang, Q. Investigation of the electrochemical and electrocatalytic behavior of single-wall carbon nanotube film on a glassy carbon electrode. *Analytical Chemistry*, 73(5):915-920, 2001.

[34] Fashedemi, O.O. and Ozoemena, K.I. Comparative electrocatalytic oxidation of ethanol, ethylene glycol and glycerol in alkaline medium at Pd-decorated FeCo@Fe/C core-shell nanocatalysts. *Electrochimica Acta*, 128:279-286, 2014.

[35] Fleischmann, M., Korinek, K. and Pletcher, D. The oxidation of organic compounds at a nickel anode in alkaline solution. *Journal of Electroanalytical Chemistry and Interfacial Electrochemistry*, 31(1):39-49, 1971.

[36] Bhunia, K., Khilari, S. and Pradhan, D. Monodispersed PtPdNi trimetallic nanoparticles-integrated reduced graphene oxide hybrid platform for direct alcohol fuel cell. *ACS Sustainable Chemistry & Engineering*, 6(6):7769-7778, 2018.

[37] Iwasita, T. Electrocatalysis of methanol oxidation. *Electrochimica Acta*, 47(22-23):3663-3674, 2002.

[38] Twigg, M.V. *Catalyst handbook*. Routledge, 2018.

[39] Cui, X., Xiao, P., Wang, J., Zhou, M., Guo, W., Yang, Y., He, Y., Wang, Z., Yang, Y., Zhang, Y. and Lin, Z. Highly branched metal alloy networks with

superior activities for the methanol oxidation reaction. *Angewandte Chemie*, 129(16):4559-4564, 2017.

[40] Amin, R.S., Hameed, R.A., El-Khatib, K.M., El-Abd, H. and Souaya, E.R. Effect of preparation conditions on the performance of nano Pt-CuO/C electrocatalysts for methanol electro-oxidation. *International journal of hydrogen energy*, 37(24):18870-18881, 2012.

[41] Stuckey, P.A., *Kinetic studies and electrochemical processes at fuel cell electrodes*. PhD thesis, Department of Chemical Engineering, Case Western Reserve University, 2011.

[42] Prasanna, D. and Selvaraj, V. Cyclophosphazene based conductive polymer-carbon nanotube composite as novel supporting material for methanol fuel cell applications. *Journal of colloid and interface science*, 472:116-125, 2016.

[43] Jeon, J.S., Yu, I.K., Kim, W. and Choi, S.H. Electrocatalytic oxidation of methanol by a polymeric Ni complex-modified electrode prepared by a one-step cold-plasma process. *Frontiers in Chemistry*, 8:595616, 2020.